



UNIVERSITY  
OF AMSTERDAM



MSc. Physics and Astronomy

Science for Energy and Sustainability

---

# Au@Pd Core@Shell Nanocube on Mirror for Plasmonic Photocatalysis

---



*Author:* Elaina Galvin

*Supervisor:* dr. Eitan Oksenberg

*Examiner:* prof. dr. Erik Garnett

*Second Examiner:* dr. Esther Alarcón Lladó

Master Thesis

60 ECTS

September 23, 2022



# *Abstract*

Globally, more than 90% of chemicals are produced by some catalytic process. Catalysts are used to reduce the activation energy barrier of reactions and enhance reaction rates. Despite their widespread use, the chemical sector is the largest industrial consumer of oil and gas. Therefore, we need more selective and efficient catalysts to reduce the sector's fossil fuel consumption and greenhouse gas emissions, with the aim of limiting global warming to 1.5°C. Plasmonic photocatalysis has emerged as a technology which utilizes efficient light harvesting abilities of plasmonic materials for more selective and enhanced catalysis. Furthermore, this technology can decrease the required energy input for high volume reactions and unlocks the potential for sunlight driven reactions. Gold nanoscale cavities in a nanocube on mirror (NCoM) configuration have shown to be a promising platform for plasmon driven chemistry. While gold has great plasmonic properties, it is not a surface active catalyst. To enhance the catalytic capabilities of the NCoM we include palladium, a more catalytically active material. Palladium is a renowned catalyst which is currently used in many industrial chemical reactions, but does not have plasmonic properties in the visible region. We exploit the synergy of gold@palladium (Au@Pd) core@shell nanostructures by fabricating a Au@Pd core@shell NCoM. We propose this construct as a platform for both plasmon enhanced catalysis and to discern the governing process of a chemical reaction. Guided by simulations of Au@Pd core@shell NCoMs, we optimize the trade-off between plasmon damping and enhanced catalysis by growing a thin Pd shell ( $\approx 2$  nm) on Au nanocubes. The precise tuneability of the NCoM is exhibited through further simulations. We fabricate Au@Pd NCoMs with a quality factor of 13.8 and show that this is a promising framework for inducing and tracking plasmon driven catalysis.

# Contents

<b>1</b>	<b>Introduction</b>	<b>1</b>
<b>2</b>	<b>Theory and Design</b>	<b>3</b>
2.1	Plasmonic Photocatalysis . . . . .	3
2.1.1	Localized Surface Plasmon Resonance . . . . .	3
2.1.2	Plasmonic Photocatalysis . . . . .	4
2.1.3	Plasmon Decay Pathways . . . . .	4
2.2	Nanocube on Mirror Configuration . . . . .	10
2.2.1	Plasmon Resonance Lineshape . . . . .	10
2.2.2	Plasmonic Nanoscale Cavity . . . . .	12
2.2.3	Resonance Tunability . . . . .	13
2.2.4	Cavity Characterisation . . . . .	15
2.2.5	Plasmon Resonance Lineshape Analysis . . . . .	15
2.3	Gold@Palladium Core@Shell Nanocube on Mirror Configuration . . . . .	18
2.3.1	Properties of Gold@Palladium Core@Shell Nanocubes . . . . .	18
2.3.2	Experiment Configuration . . . . .	22
<b>3</b>	<b>Methods</b>	<b>24</b>
3.1	FDTD Simulations . . . . .	24
3.2	Palladium Shell Overgrowth . . . . .	25
3.2.1	Chemicals . . . . .	25
3.2.2	Synthesis . . . . .	25
3.2.3	Optical Characterisation . . . . .	27
	UV-VIS Spectroscopy . . . . .	27
3.2.4	Elemental Characterisation . . . . .	28
	Transmission Electron Microscope - Energy Dispersive X-Ray Spectroscopy (TEM-EDS) . . . . .	28
	Scanning Electron Microscope - Energy Dispersive X-Ray Spec- troscopy (SEM-EDS) . . . . .	28
3.2.5	Structural Characterisation . . . . .	29
	High Angle Annular Dark Field - Scanning Transmission Elec- tron Microscopy (HAADF-STEM) . . . . .	29



	High Resolution Transmission Electron Microscopy (HRTEM) . . . . .	29
	Particle Size Distribution . . . . .	29
3.3	Nanocavity Fabrication . . . . .	30
3.3.1	Chemicals . . . . .	30
3.3.2	Substrate Preparation . . . . .	30
	Base Piranha . . . . .	30
	Plasma Cleaning . . . . .	30
3.3.3	Fabrication . . . . .	30
	Spin Coating . . . . .	30
	UV-Lithography . . . . .	31
	Thermal Evaporation . . . . .	31
	Lift-Off . . . . .	31
	Atomic Layer Deposition (ALD) . . . . .	31
	Dropcasting . . . . .	32
3.3.4	Characterisation . . . . .	32
	Integrating Sphere Spectroscopy . . . . .	32
	Cathodoluminescence (CL) . . . . .	34
3.4	Plasmon Driven Reaction on a Single Nanocavity . . . . .	35
3.4.1	Ligand Exchange . . . . .	35
3.4.2	Lineshape Analysis . . . . .	35
<b>4</b>	<b>Results and Discussion</b>	<b>36</b>
4.1	FDTD Simulations . . . . .	36
4.1.1	UV-VIS Spectroscopy Simulations . . . . .	36
4.1.2	Effect of Pd Shell Thickness in NCoM . . . . .	37
4.1.3	Effect of Dielectric Spacer Thickness in NCoM . . . . .	39
4.1.4	Effect of Gold Core Dimensions in NCoM . . . . .	40
4.2	Pd Shell Overgrowth . . . . .	40
4.2.1	Optical Characterisation . . . . .	40
4.2.2	Elemental Characterisation . . . . .	41
4.2.3	Structural Characterisation . . . . .	42
4.3	Nanocavity Characterisation . . . . .	45
4.3.1	Fabrication Results . . . . .	45
4.3.2	Quality Factor . . . . .	46
4.3.3	NCoM Modes . . . . .	47
4.4	Plasmon Driven Chemistry . . . . .	49
4.4.1	Controls . . . . .	49
	Conduct Linescans on Cavities Prior to Ligand Exchange . . . . .	49

Surface Enhanced Raman Spectroscopy Measurement to Confirm Ligand Exchange . . . . .	49
Induce Reaction on Au Nanocavities . . . . .	49
4.4.2 Measurements . . . . .	50
Measurement Analysis . . . . .	50
<b>5 Conclusions and Outlook</b>	<b>53</b>
<b>Bibliography</b>	<b>55</b>
<b>Acknowledgements</b>	<b>63</b>
<b>A Measurement Data from Section 4.4.2</b>	<b>64</b>

# Chapter 1

## Introduction

The term catalysis broadly defines a process where the rate and/or products of a reaction are changed due to the presence of a substance, which is called the catalyst [1]. Globally, more than 90% of chemicals are produced by some catalytic process, with catalysis contributing to about 30% of the world's total gross domestic product, making it one of the largest global industries [2]. Although using a catalyst reduces the activation energy barrier required to go from reactants to products, it does not remove it [3]. In conventional catalytic reactions, high temperatures and pressures are required to overcome this barrier. Typically, this energy is sourced from fossil fuels, making the chemical sector the largest consumer of oil and gas compared with any other industry. However, it is listed as third in terms of emissions due to half of the fossil fuels consumed are used as feedstock for products [4]. Products like plastics store the carbon until the end of the product's life, resulting in an underestimation of the sector's carbon emissions.

The IPCC Report 2022 reiterated the goals of the Paris Climate Agreement, that global warming must be limited to an average of 1.5°C compared with pre-industrial times to avoid the catastrophic impacts further warming will cause [5]. To achieve this goal 'net-zero' emissions must be obtained by 2050, which means that the anthropogenic emission of greenhouse gases must be balanced by anthropogenic removal of the gases [6]. Currently, efficient carbon capture and storage techniques are limited; therefore, a huge effort must be placed in reducing emissions as much as possible across all sectors.

One strategy to lower the emissions of the chemical industry is to use catalysts that are more efficient and selective. Doing so results in reactions occurring faster and requiring a lower energy input, accompanied by fewer harmful by-products. The second strategy is to use electricity generated from renewable energy sources to drive reactions. Plasmonic photocatalysis harnesses both ideas into one platform, allowing for efficient, selective chemistry at ambient conditions. In this framework, visible light is used as the energy source to overcome the activation energy barrier. This energy can be generated from renewably produced electricity and furthermore allows for the possibility of driving chemistry using our most abundant energy source, the sun. This field

has huge potential for sustainable chemistry, however there are gaps in the fundamental knowledge required to optimize reactions due to the short timescale of plasmonic processes.

Herein, a platform is proposed to be used for both the enhancement of plasmonic catalysis and to discern the governing process of a chemical reaction. Included in this work are simulations of gold-palladium (Au@Pd) core-shell nanocube on mirror (NCoM) systems, used to understand the trade-off between plasmon damping and a catalytic surface. Furthermore, they provide information on the precise tuneability of the NCoM. The procedure for a thin palladium (Pd) shell overgrowth on gold (Au) nanocubes is exhibited and characterised, followed by Au and Au@Pd core@shell nanocavity fabrication and characterisation. Finally, the processes of inducing and analysing a plasmon driven reaction in the NCoM construct are shown and discussed.

## Chapter 2

# Theory and Design

## 2.1 Plasmonic Photocatalysis

### 2.1.1 Localized Surface Plasmon Resonance

Plasmonic metal nanoparticles are nanoscale (on the order of  $10^{-9}\text{m}$ ) materials that can efficiently absorb and scatter incident light [7]. Light incident on a nanoparticle is considered resonant when it induces the largest optical response possible from the nanoparticle. In other words, resonance is achieved when the wavelength of the incident light matches the frequency of electron oscillations in the nanoparticle. When resonant light is directed on the particle a strong interaction arises between the conduction band electrons and the electromagnetic field (the light) [8]. A collective oscillation of conduction band electrons is generated, oscillating in resonance with the light, and remains localised to the surface of the metal as shown in Figure 2.1 [9]. The restoring force due to the displacement of the electrons gives rise to a resonance which is specific to the material and geometry [10]. This phenomenon is known as a localised surface plasmon resonance (LSPR).

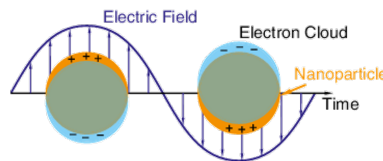


FIGURE 2.1: Schematic of LSPR [11]

To understand the conditions for a LSPR the material's optical properties must be considered. The optical properties of metals are described by a complex dielectric function given by  $\epsilon(\omega) = \epsilon_1(\omega) + i\epsilon_2(\omega)$ , which depends on the frequency of incoming light [12].

The dielectric function conditions for a plasmon resonance to occur are [13];

$$\epsilon_1(\omega)\epsilon_2(\omega) < 0 \quad (2.1)$$

$$\epsilon_1(\omega) + \epsilon_2(\omega) < 0 \quad (2.2)$$

It should be noted to derive these conditions it is assumed that the imaginary part of the dielectric function for both the metal nanoparticle and the surrounding medium are assumed to be small and are consequently neglected. The conditions obtained in equations 2.1 and 2.2 incur that the dielectric function of the material must be negative and have a larger absolute value than the surrounding medium. Coinage metals like gold, silver and copper have a large negative real part of the dielectric function with a small imaginary part [13]. Accordingly, these metals are good materials to host plasmon resonances, however the exploration of non-coinage plasmonic materials is increasing [14–16].

### 2.1.2 Plasmonic Photocatalysis

Plasmon driven chemistry has emerged as an exciting field to combine the efficient light harvesting of plasmonic materials with their ability to distribute energy and charge to an adjacent or adsorbed molecule [17]. The idea is that reactions can be induced and/or catalysed on the surface of a metal nanoparticle using visible light induced plasmon resonances [9]. Unlike conventional catalysis, plasmon enhanced chemistry, i.e. plasmonic photocatalysis, can be carried out at ambient conditions [18]. Therefore, using light to drive chemistry in industry could have a huge impact on the quantity of greenhouse gases emitted, since high temperatures and pressures are not required. Furthermore, it allows for the possibility to utilize our most abundant energy source, the sun, to drive industrial chemical reactions. Plasmonic photocatalysis also provides a platform for carrying out reactions with higher product selectivity and enhanced reaction rates [18]. The mechanisms allowing for these improvements will be discussed in the following sections.

### 2.1.3 Plasmon Decay Pathways

To realize the full potential of plasmonic photocatalysis and bring the technology to the chemical industry it is critical to discern the fundamental process governing the reaction in question. This, in turn, allows for efficient exploitation of systems to produce the desired products and avoid unwanted by-products. Recognizing key steps in a reaction procedure also allows for the energy input to be minimized by inputting only

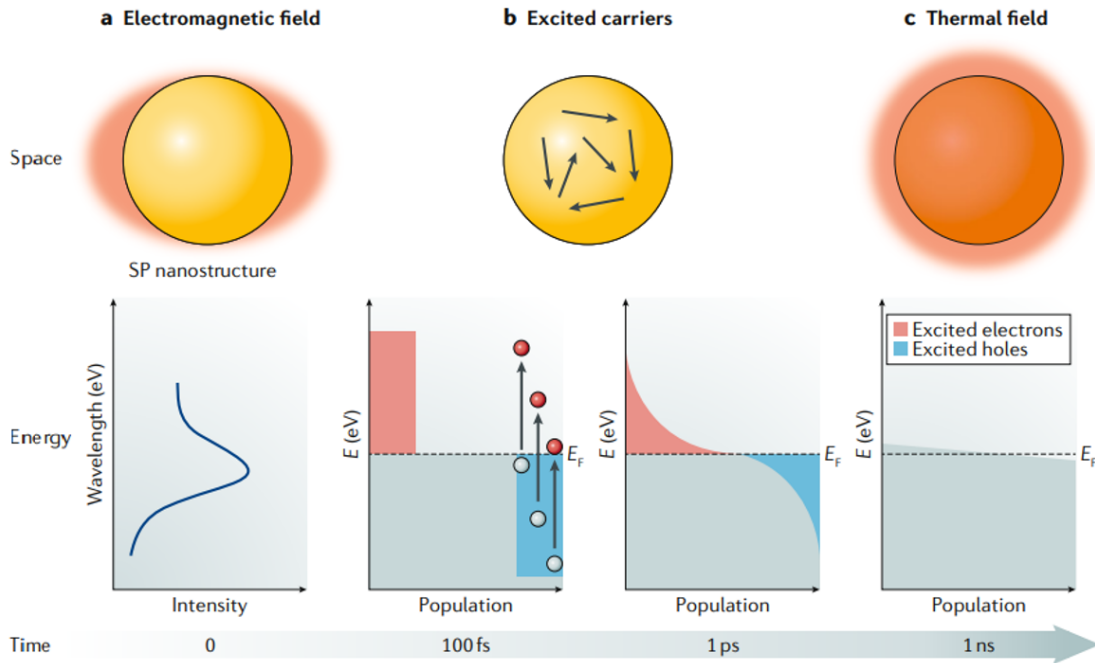


FIGURE 2.2: Schematic of decay pathways of localized surface plasmon resonance, obtained from [21], adapted from [22] and [23]

the requirement to induce desired process. Despite that plasmon enhanced catalysis has been successfully exhibited by multiple groups [19, 20], the mechanism driving the reaction is often debated. The decay pathways of surface plasmons have unique and interesting properties and typically more than one of these will play a role in a reaction process, making it difficult to pinpoint the driving mechanism. Plasmon decay pathways include enhanced near fields, hot carrier generation, and photothermal heating.

### *Enhanced Near Fields*

Due to the fundamental laws of diffraction, dielectric lenses cannot focus light into regions less than about half the wavelength of incident light ( $\approx \lambda/2$ ) [24]. However, plasmonic nanoparticles can concentrate incident radiation into sub-wavelength dimensions, overcoming the diffraction limit [8]. This is explained by using the quasi-static approximation to describe the interaction of a spherical nanoparticle of size  $a$  with an external electromagnetic field. This approximation only holds when the size of the particle  $a$  is much smaller than the wavelength of light ( $a \ll \lambda$ ), which is true for nanoparticles with dimensions less than 100 nm. Since the phase of the field oscillating over the nanoparticle is much larger than the particle itself, the particle can be approximated to be in a homogeneous, static field [13]. Assuming that polarization of

the material due to the field is small, so  $E = E_{in}$  the local dipole moment is given by;

$$\mathbf{P} = \epsilon_0 \chi_e \mathbf{E}_{in} \quad (2.3)$$

Where  $\epsilon_0$  is the free space permittivity and  $\chi_e$  is the electric susceptibility a material property given by  $\epsilon_r(\omega) - 1$ , where  $\epsilon_r(\omega)$  is the relative permittivity. Using the quasi-static and polarizability assumptions the total dipole moment is given by [25],

$$p = \int_V \epsilon_0 \chi_e \mathbf{E}_{in} dV = \epsilon_0 V (\epsilon_r(\omega) - 1) \mathbf{E}_{in} \quad (2.4)$$

Where  $V$  is the particle volume. To understand the field generated as a result of the polarization, Poisson's equation,  $E = \nabla \Phi = 0$  is applied. Under the assumptions that (1) there is no excess charge on the surface of the particle (2) the potential across the sphere boundary is continuous and (3) there is a jump in the slope, the potential inside and outside the particle can be derived to give [25];

For ( $a < r$ )

$$\Phi_{in} = - \left( \frac{3\epsilon_m}{\epsilon_r(\omega) + 2\epsilon_m} \right) E r \cos \theta \quad (2.5)$$

For ( $a > r$ )

$$\Phi_{out} = - E r \cos \theta + \frac{p \cos \theta}{4\pi \epsilon_m r^2} \quad (2.6)$$

Where  $a$  is the sphere radius and  $r$  is the distance from the centre of the sphere,  $\epsilon_m$  is the relative permittivity of the surrounding medium and  $\epsilon_r(\omega)$  is the relative permittivity of the nanoparticle. Equations 2.5 and 2.6 imply that the induced field inside the particle (2.5) is homogeneous, while the field outside the sphere (2.6) is comprised of the incident field with the addition of the field induced by the dipole. Since  $\lim_{r \rightarrow \infty} \Phi_{out}(r) = -E r \cos \theta$ , the enhanced field due to the dipole exists near the surface of the nanoparticle.

Furthermore, plasmonic materials can harvest light over a larger volume than their physical size. The dipole moment of the nanosphere is proportional to the electric field,  $p = \alpha E$ , with constant term  $\alpha$  described as the polarizability [25]. Since the dipole is in a static field, the quasi-static polarizability constant of a small sphere of volume  $V$  can be approximated as [13];

$$\alpha = 3\epsilon_0 \epsilon_m V \frac{\epsilon_r(\omega) - \epsilon_m}{\epsilon_r(\omega) + 2\epsilon_m} \quad (2.7)$$

Where  $V = \frac{4}{3}\pi r^3$ . The dipole moment of the nanosphere is now described by;

$$\vec{p} = 4\pi \epsilon_0 R^3 \frac{\epsilon_r(\omega) - \epsilon_m}{\epsilon_r(\omega) + 2\epsilon_m} \epsilon_m \vec{E}_0 \quad (2.8)$$



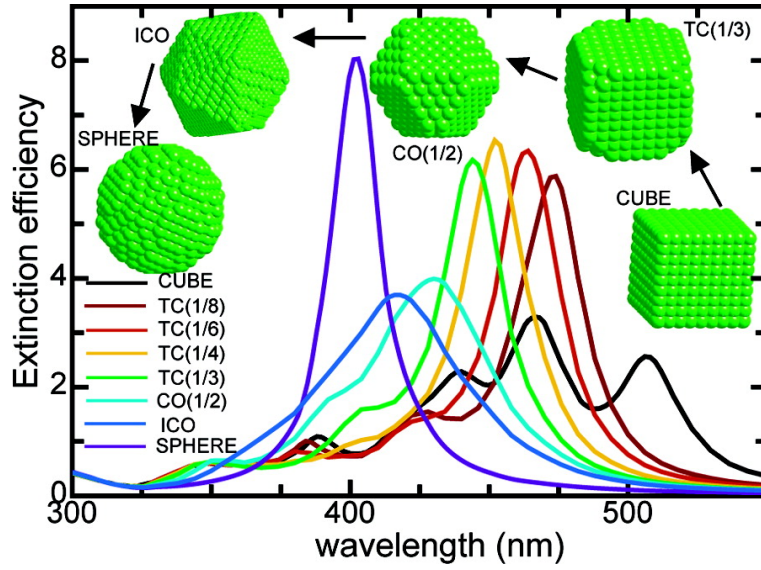


FIGURE 2.3: Extinction efficiency for various nanoparticle shapes of silver nanocubes [26]

To maximize polarizability, and thus obtain resonant enhancement, the denominator  $|\epsilon(\omega) + 2\epsilon_m|$  should be minimized. Subbing this condition ( $\epsilon(\omega_0) = -2\epsilon_m$ ) into the equation 2.7, the resulting polarizability of the sphere exceeds its volume by about a factor of 9. Experimentally, the extent of polarizability or the magnitude of the dipole moment induced is measured through the extinction cross section, which describes the relationship between the power removed from the beam and the incident intensity, in units of area. Plasmonic nanoparticle's large extinction cross section is due to the strong interactions between the conduction band electrons and the incoming light which induces a the strong polarizability, which is maximized at the resonant frequency. Although the above equations are modelled on a spherical nanoparticle, a large extinction cross section can be obtained for an array of nanoparticle geometries which is shown in Figure 2.3, where extinction efficiency is a term described by  $Q_{ext} = \frac{\sigma_{extinction}}{\sigma_{geometric}}$ . A particle with an extinction efficiency of 8, such as the sphere in Figure 2.3, casts a shadow 8 times larger than its physical size.

According to equation 2.6 the induced electric field due to the dipole remains on the surface of the particle and thus the light is concentrated into very small volumes. This, combined with their large extinction cross section supports drastic electromagnetic field enhancements on the surface of the particle (fig 2.4).

When the energy of the incident radiation is resonant and matches the electronic transition of the adsorbed molecule, or a molecule in the near vicinity of the nanoparticle, the excitation probability of the molecule is increased due to the enhanced field [28]. That is to say, the extinction spectrum of the nanoparticle must overlap with that of the adsorbed molecule to observe a near field driven reaction as shown in Figure 2.2

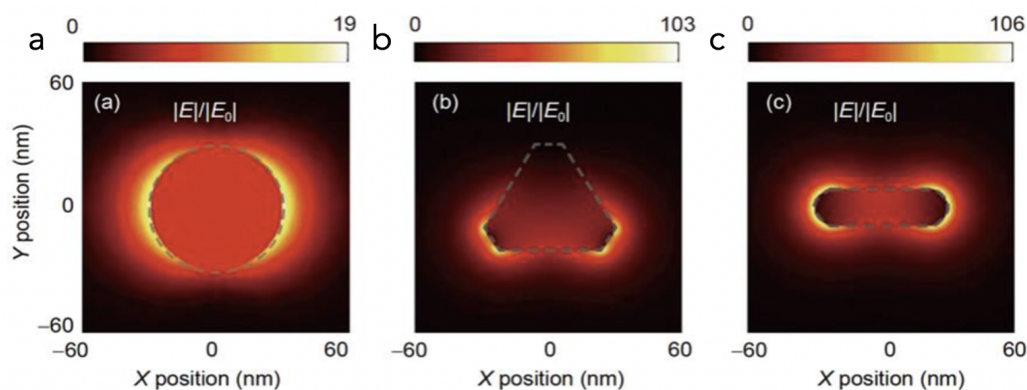


FIGURE 2.4: Enhanced near field simulations of various shapes of silver nanoparticles [27]

a. This process happens on the time scale of 1-100 fs [21].

### Hot Carrier Generation

Plasmonic nanoparticles convert light energy into excited carriers which can then be transferred non-radiatively to an adsorbate molecule. There are two types of these excited carriers. The first are high energy, or 'hot' electrons and holes, which have energies larger than thermal excitation at ambient temperature and can induce charge driven enhanced catalysis [29]. Hot electrons have an energy of  $+h\nu$  and hot holes have an energy of  $-h\nu$  with respect to the Fermi level of the metal [30]. For ease of discussion, only hot electrons will be considered in further sections. The damping of hot electrons is a quantum mechanical process which happens at the surface of nanoparticles, namely Landau damping, on a timescale of 1-100 fs [29]. After a resonant beam is directed on a particle, a plasmon quantum from the hot electron can be transferred to create an excited carrier, an electron-hole pair [7]. Through these interactions, the hot electrons go from a non-thermal distribution and thermalize to a Fermi-Dirac distribution [31]. The lower energy electrons that gain energy can be termed 'warm' and are the electrons taking part in catalysis. The second excited carriers are frictional carriers with excitation energies near the Fermi level and can be described by the Drude model [32]. These are lower in energy and are responsible for the LSPR.

There are two mechanisms in which warm electrons can induce charge driven catalysis, namely indirect and direct, shown in Figure 2.5. In the indirect mechanism the warm electrons leave the metal and enter the lowest unoccupied molecular orbital (LUMO) of the adsorbed molecule if they gain the required energy for the transition as shown in Figure 2.5 a [29]. This can induce a charged state in the adsorbate [31]. The charged state has a new potential energy surface which determines the chemical

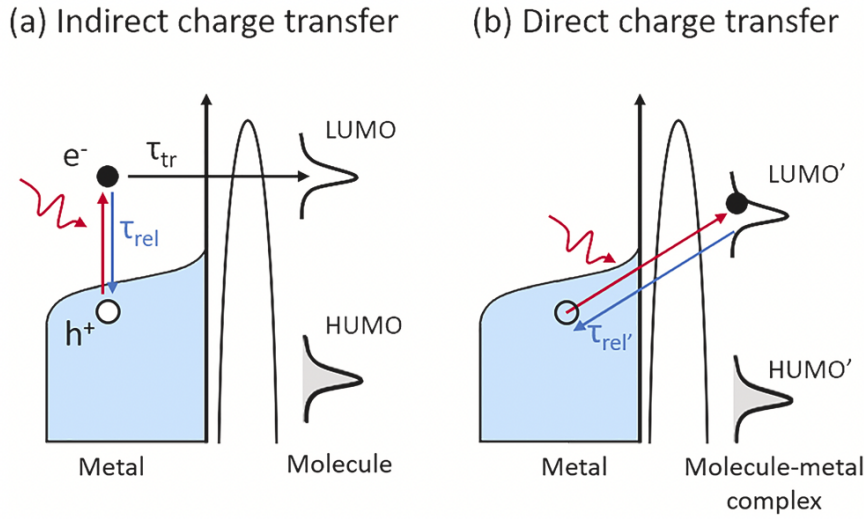


FIGURE 2.5: Schematic of (a) indirect and (b) direct charge transfer mechanism [33]

reaction, thus the molecules on the surface can undergo a chemical reaction with an altered chemical pathway. The efficiency of the indirect charge transfer mechanism follows the equation [34];

$$ef f_{(\omega)} = \frac{rate_{e(h)}(\omega)}{(\sigma_{NC} I_0 / \hbar \omega)} = \gamma_{tun} \frac{\delta n_{e(h)}(\epsilon_{mol}, \omega)}{n_{DOS}(\epsilon_{mol}, \omega)} \quad (2.9)$$

Where  $\delta n_{e(h)}$  is the average number of excited electrons with the LUMO energy  $\epsilon_{mol}$ ,  $\gamma_{tun}$  is the tunneling rate,  $\sigma_{NC}$  absorption cross section of the metal nanoparticle, and  $n_{DOS}(\epsilon_{mol})$  density of states of the metal nanoparticle at  $\epsilon_{mol}$ . Since the equation depends on the number of carriers with sufficient energy to enter the LUMO of the adsorbate, it is expected that an increase in photon energy (lower wavelengths) incident on the particle should increase the indirect charge transfer efficiency due to the generation of more electrons with adequate energy.

In the direct regime, plasmon dephasing promotes charge transfer directly from the metal to the LUMO of an adsorbed molecule. This is possible due to the formation of a molecule-metal complex shown in Figure 2.5 b. Consider a system comprised of a molecule adsorbed to a metal nanoparticle with hybridized orbitals. The electron-accepting states of this hybridization are centred on the molecule, while the donating hybridized states are centered on the metal. Direct electron transfer is possible in this system as the hot electrons go directly from the donating state of the metal to the acceptor states of the molecule [35]. The hot electron then thermalizes through electron-electron scattering in the adsorbed molecule and either distributes its energy to electrons in the adsorbate or creates a charged state, which like in the indirect regime, can induce a reaction. However, in this regime it is expected that increasing

photon energy may not lead to direct enhancements in electron transfer efficiency, since this mechanism depends on the complex formed between the molecule and metal. It is the enhanced field that drives the electron transfer between the metal and molecule. However, contrary to near field driven reactions, hybridized metal-molecule states are a prerequisite.

### *Photothermal Heating*

The final mechanism is photothermal heating. The electrons further thermalize through electron-phonon interactions on a timescale of 100 ps-10 ns. The lattice temperature increases followed by heat dissipation into the environment [29]. For both near field enhanced and hot-carrier assisted plasmonic photocatalysis, the rate of a chemical transformation is proportional to the rate of incident photons under moderate power continuous wave (CW) illumination [36]. However, in photothermal driven reactions, a linear dependence of power is not expected. A photothermal driven reaction can be described using the Arrhenius equation;

$$K = A \exp(-E_a/RT) \quad (2.10)$$

Where  $K$  is the reaction rate,  $A$  is a pre-exponential constant,  $E_a$  is the activation energy,  $R$  is the universal gas constant and  $T$  is the temperature. Due to the approximation that the temperature increase of a nanoparticle due to the absorption of a photon is proportional to the power of the laser on the sample and the extinction cross section, the reaction rate should follow an exponential trend [36]. However, to deduce a reaction mechanism by simply changing the laser power is not always trivial. To do so, a large range of laser powers must be used. This can be problematic because at high powers other effects can play a role such as changes in catalyst surface coverage and convection effects.

## **2.2 Nanocube on Mirror Configuration**

### **2.2.1 Plasmon Resonance Lineshape**

The lineshape of a plasmon resonance describes the width, intensity, and resonant energy of the extinction spectrum shown in Figure 2.6. The ability to tune the plasmon resonance of a metal nanoparticle is beneficial as it provides a pathway to regulate both the electronic and optical properties of the particle. However, through the size and shape dispersity of colloidal solutions of nanoparticles, inhomogeneous broadening of the plasmon resonance lineshape occurs. Particles of different sizes have slightly different optical properties and thus have varying spectral shapes. One method to

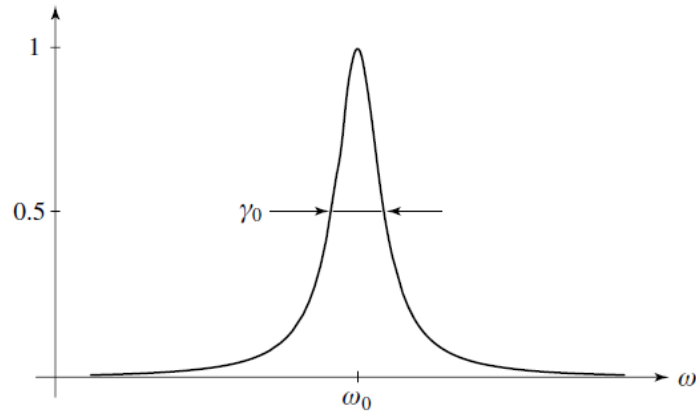


FIGURE 2.6: Plasmon resonance lineshape [13]

overcome inhomogeneous broadening is to conduct studies on a single particle level, thus avoiding ensemble averaging and obtaining a homogeneous lineshape which characteristic of the specific nanoparticle.

Owing to losses brought about by the damping constant of the plasmon decay, plasmonic systems are non conservative [13]. To understand the effect of plasmon damping on the resonant lineshape, the transfer of the energy quanta from the hot electron the lower energy electrons can be described using the undriven harmonic oscillator model. The transfer of the energy quanta, the plasmon decay, can be considered as the radiation that is emitted by an undriven harmonic oscillator. The undriven harmonic oscillator's dipole moment is restored when it loses its energy to the radiation field, comparable to the hot electrons thermalizing. Using the undriven oscillator model the following energy-frequency relation can be derived [13];

$$\frac{dW}{d\Omega d\omega} = \frac{1}{4\pi\epsilon_0} \frac{|\mu|^2 \sin^2(\theta) \omega_0^2}{4\pi^2 c^3 \gamma_0^2} \left[ \frac{\gamma_0^2/4}{(\omega - \omega_0)^2 + \gamma_0^2/4} \right] \quad (2.11)$$

Where  $\frac{dW}{d\Omega d\omega}$  is the total energy per unit angle per unit frequency and  $d\Omega = \sin\theta d\theta d\phi$ .  $\mu$  is the collective dipole moment,  $\omega_0$  is the resonance frequency and  $\omega$  is the incoming frequency.  $\gamma_0$  is the damping term, where  $\gamma_0 = \frac{1}{\tau_0}$  and  $\tau_0$  is the lifetime of the oscillator. Note that for this approximation to hold  $\gamma_0 \ll \omega_0$  must hold true. The final term in the square brackets of equation 2.11 determines the shape of the function, which follows a Lorentzian lineshape function [13]. The relationship between decay rate and the linewidth follows Heisenberg's uncertainty principle,  $\Delta E \Delta t \approx \hbar$ , where the linewidth defines the energy uncertainty  $\Delta E = \hbar \Delta\omega$  and the measurement time of the excitation is related to the decay time and thus the damping,  $\Delta t \approx \frac{1}{\gamma_0}$ . Now;

$$\Delta E \Delta t = \hbar \omega \frac{1}{\gamma_0} \approx \hbar \quad (2.12)$$

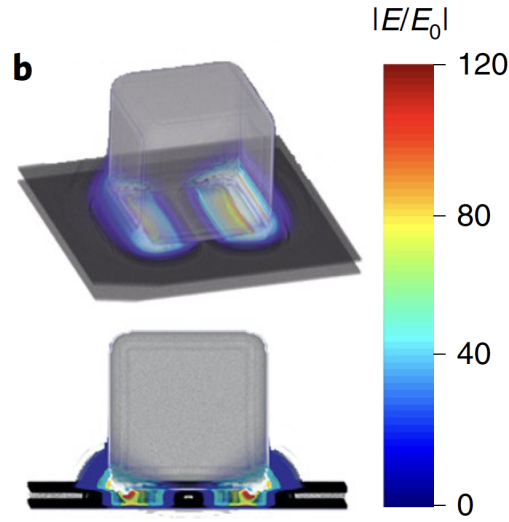


FIGURE 2.7: Simulation of nanocube on mirror with intense electric field enhancement in the gap [38]

Therefore,

$$\Delta\omega \approx \gamma_0 \quad (2.13)$$

Where  $\Delta\omega$  is the full width of the Lorentzian function at half the maximum (FWHM) of the curve. Accordingly, changes in the linewidth of the resonance provide information about the plasmon decay.

### 2.2.2 Plasmonic Nanoscale Cavity

Plasmonic nanoscale cavities are an ideal platform for studying single particle level systems due to the unprecedented light confinement and enhanced field in the cavity (Fig 2.7). On account of the confinement, a relatively high measurement signal can be acquired for a single particle system. The nanocube on mirror (NCoM) configuration is a plasmonic nanoscale cavity framework. The system is made up of three constituents, a mirror covered by a thin dielectric spacer and a nanoparticle on top. The nanoscale cavity lies between the nanoparticle and mirror. The cavity acts as a waveguide allowing for multiple reflections of the mode in the gap [37].

The NCoM system can be fabricated with great precision due to the availability of a highly accurate method of depositing the dielectric spacer, namely atomic layer deposition. The nanocavity's small size allows for a large free spectral range, which means that for each cavity length only two mode orders are seen in the visible range [39]. The first order, 'gap' mode, is broken into discrete states,  $s_{m,n}$  where  $m$  is the radial node and  $n$  is the azimuthal node. These nodes depend on the geometry of the NCoM and have poor coupling efficiency to free space. However, when the NCoM has the correct symmetry, the second order mode, the 'antenna' mode  $l$ , can couple with the

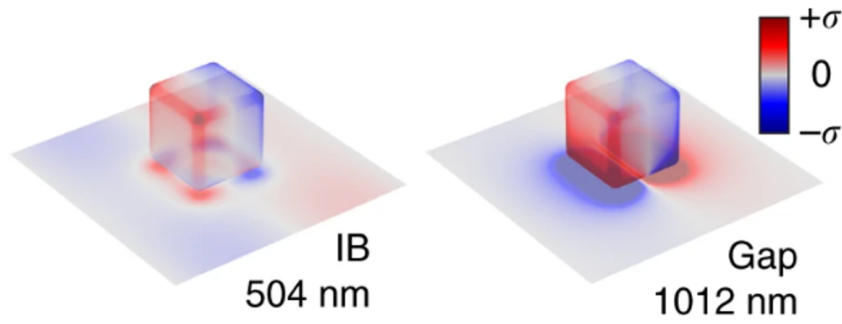


FIGURE 2.8: Charge distribution of silver NCoM, showing interband (IB) and gap mode [44]

gap mode creating mixed modes,  $s_{m,n} + l = j_n$  [40]. Consequently, it is not possible to separate the system into 3 components because the system becomes a hybridization of the Fabry-Perot gap mode and antenna mode. When the system is resonantly excited charge oscillations (dipoles) on the nanoparticle couple to image charges on the mirror which hybridize and form a symmetric longitudinal gap mode perpendicular to the surface [41, 42]. This highly confined trapped mode generates an extremely sharp, strong, and tuneable plasmon resonance in the gap [38, 43]. The coupling of the cavity mode with the nanoparticle's antenna mode then radiates effectively due to the charge distribution over the entire nanosystem [41]. The charge distribution in the NCoM depends on which mode is excited as shown in Figure 2.8 [44]. The first cube in Figure 2.8 represents the charge distribution due to interband transitions, which is at about 504 nm for this silver nanocube on mirror. The charge is mostly concentrated on the four corners of the nanocube. The latter cube displays the gap mode at 1012 nm and is mostly concentrated along two sides of the cube.

### 2.2.3 Resonance Tunability

The NCoM is a highly tunable construct, with the resonant lineshape dependent on the size and shape of the nanoparticle, and the thickness of the spacer. Figure 2.9a shows the extinction spectra of four separate Au NCoMs. Due to changes of just a few nanometers of the Au nanocubes the resonance lineshape varies. This is due to the different confinement of conduction band electrons which plays a role in the optical properties through both the position and width of the resonance [45]. For a particle that is larger than the mean free path of the conduction band electrons size increases, the plasmon linewidth is expected to increase. This characteristic is attributed to an increase in radiation damping with increasing particle size. Furthermore, a red shift is expected with increasing nanoparticle size. Consider the same nanoparticle in an



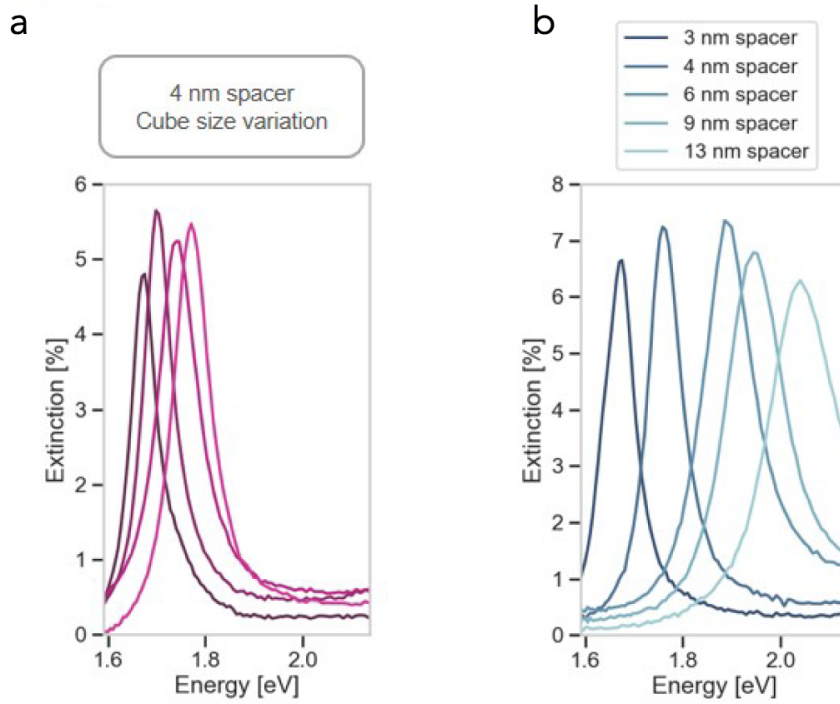


FIGURE 2.9: Extinction measurements of gold NCoM (a) with varied gold cube sizes and (b) varied spacer thickness [38]

electric field as a dipole. As the particle size increases there is a weaker interaction between the charges since they are further apart, and thus it has a smaller dipole moment. The restoring force depends on how strongly the charges feel each other due to Coulomb interactions drawing the electrons back together. The stronger the Coulomb interaction, the higher the frequency oscillations required to sustain the resonance. Due to the inverse relationship between frequency and wavelength  $\lambda \propto \frac{1}{\omega}$ , large particles require low frequencies to maintain the oscillation thus a red spectral shift is observed. For small particles, higher frequencies are required to sustain the resonance, thus a blue shift is seen for smaller particles. However, this trend is not always observed experimentally [45].

Moreover, the NCoM is closer to a Fabry-Perot cavity than a plasmonic nanoparticle, and so changing the space between the mirrors dominates the gap mode's properties. The thickness of the spacer (gap size) plays a critical role in the resonant energy lineshape, allowing the resonant energy to span over a broad energy range shown in Figure 2.9b [38]. A blue shift of the gap mode with a constant gap material is assigned to an increase in gap size. The blue shift is accredited to a reduction in coupling strength of the cavity to the electric field [46].



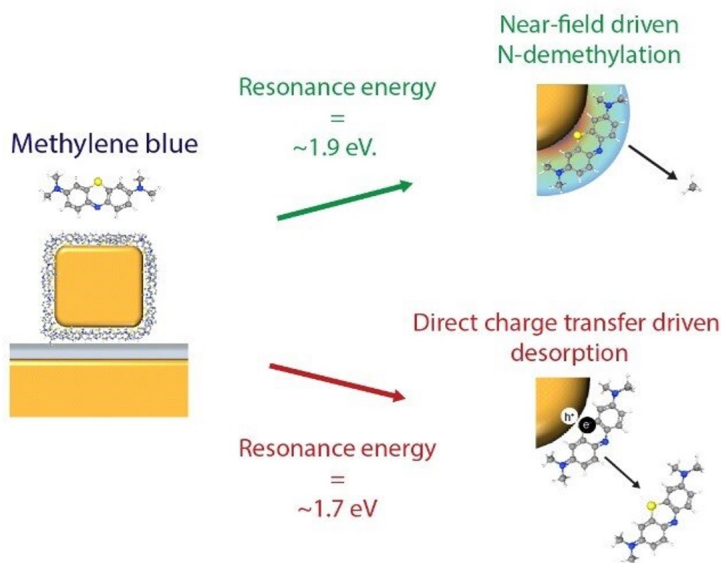


FIGURE 2.10: Energy resolved plasmon driven chemistry exhibited on gold NCoM [38]

## 2.2.4 Cavity Characterisation

A key parameter used to characterise optical cavities is the quality factor,  $Qfactor$  [47]. The quality factor represents spectral confinement in the cavity, and is described by [47];

$$Qfactor = \frac{\omega_r}{\Delta\omega} \quad (2.14)$$

Where  $\omega_r$  is the resonance frequency and  $\Delta\omega$  is the FWHM. In essence, the quality factor describes how long a photon is trapped in the cavity and is dependent on the optical feedback mechanism. In the NCoM, it is defined by the mirror and nanocube reflectivity and losses. Although extremely high mode confinement is obtained in plasmonic nanocavities, the quality factor can be reduced due to scattering losses of the nanoparticle [39].

## 2.2.5 Plasmon Resonance Lineshape Analysis

The NCoM is a powerful construct to study reactions on a single particle scale. Ok-senberg et al. used a Au NCoM to resolve reaction processes on an energy scale shown in Figure 2.10 [38]. By varying the thickness of the dielectric spacer, and using size dispersity of colloidal nanocubes to their advantage, they could uncover at what energy a reaction process occurred at, and further what the driving mechanism was for each process by spanning over a large energy range (1.6-2.1 eV). They directed a laser beam on a single NCoM and scanned over a broad range of wavelengths. This process allowed them to both induce processes at the surface of the particle, and track processes by measuring changes the nanocube's extinction spectrum for each wavelength scan.

As discussed in section 2.1.3, there are multiple decay pathways for plasmons which could drive a reaction. The total decay accounting for these mechanisms follows the equation [48];

$$\Gamma_{tot} = \gamma_{bulk} + \Gamma_{rad} + \Gamma_{surf} \quad (2.15)$$

Where  $\gamma_{bulk}$  refers to bulk damping due to the decay of the plasmon through the generation of electron-hole pairs and is described by the metal's dielectric function  $\Gamma_{rad}$  refers to the radiative decay of the plasmons, and  $\Gamma_{surf}$  describes surface scattering. These damping terms can be described using analytical and numerical electromagnetic simulations. However, it was found that the measured plasmon resonance did not match exactly with theoretically calculated resonances [49]. It was concluded that there is some additional damping mechanism, which is termed  $\Gamma_{CID}$ , which describes chemical interface damping[48],

$$\Gamma_{CID} = A \frac{\nu_f}{l_{eff}} \quad (2.16)$$

Where  $\nu_f$  is the fermi velocity of the electrons and  $l_{eff}$  is their average distance from the surface and  $A$  is a constant. The total plasmon damping is now described by;

$$\Gamma_{tot} = \gamma_{bulk} + \Gamma_{rad} + \Gamma_{surf} + \Gamma_{CID} \quad (2.17)$$

Chemical interface damping accounts for additional damping channels for the plasmon due to its surrounding environment. Thus, it is not accounted for in optical simulations that do not include ligands or adsorbates on the surface. Tracking changes in the CID can provide information about groups attached the metal. Liyanage et al. found a correlation between the nature of a group for electron donating or electron withdrawing with changes in the resonant wavelength [50]. An electron donating group is a group that increases the electron density of the molecule it is attached to, where an electron withdrawing group decreases the electron density of the molecule it is attached to. According to the Drude model, attached ligands that are electron donating should increase the free carrier concentration and therefore display a blue shift in the resonance since more free carriers increase the bulk plasmon resonance, and vice versa for electron withdrawing groups. However, the opposite trend is seen, as shown in Figure 2.11, where more electron donating groups red shift the plasmon resonance. The attached ligand is attributed to the changes to the delocalization of the electron wavefunctions due to hybridized orbitals formed between electronic states. This is possible when there is a correct alignment of the molecular orbitals. The hybridization alters the free carrier concentration of the metal nanoparticle consequently impacts the LSPR.

Oksenberg et al. observed extraordinary changes in the lineshape of cavities simply due to a change in the adsorbed ligands (Fig 2.12). This highlights the importance

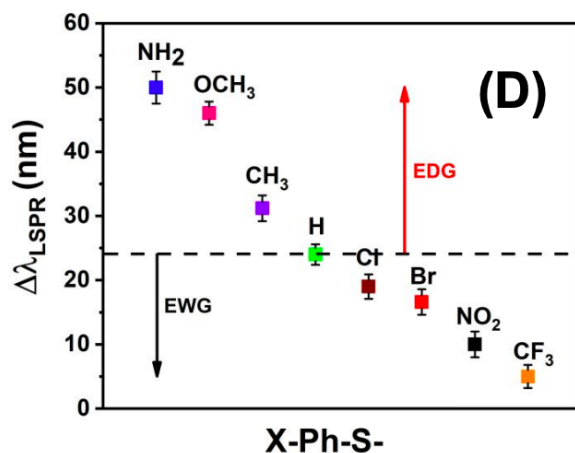


FIGURE 2.11: Change in lineshape due to ligand exchange correlated with electron withdrawing/electron donating nature of the ligand [50]

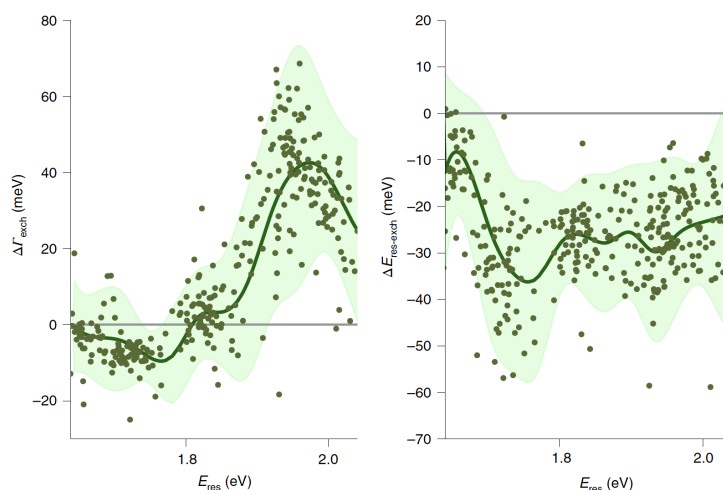


FIGURE 2.12: Change in lineshape due to ligand exchange (a) change in FWHM (b) change in resonant energy for gold NCoM

of the effect of adsorbed ligands and the influence CID has as an additional plasmon decay channel. The group tracked reactions by carrying out consecutive wavelength scans on a single cavity to induce a reaction and used changes in the lineshape to monitor processes occurring on an energy scale. Knowledge gained from the reactivity landscape of methylene blue obtained through lineshape analysis integrated with the correlation of the landscape to methylene blue's band structure was used to understand at what energy reactions were happening and what mechanism was driving the reaction. Surface Enhanced Raman Spectroscopy (SERS) was used to identify products at the energies where the largest change in lineshape were observed. Combining all of this information, the group deduced that two reaction mechanisms occurred; direct charge transfer induced desorption at 1.7 eV and near field driven demethylation at 1.9 eV (Fig 2.10). This work is remarkable not only because it provides a system to study

processes on the nanocavity's surface, which are often difficult to discern from bulk processes, but also opens the possibility to unlock and tune reaction pathways that may not be possible using conventional catalysis.

## 2.3 Gold@Palladium Core@Shell Nanocube on Mirror Configuration

### 2.3.1 Properties of Gold@Palladium Core@Shell Nanocubes

Au NCoMs exhibit intense, sharp and highly tuneable gap plasmon resonances as discussed in 2.2.5 [38]. Nonetheless, Au is not an exceptional catalyst because it does not have the correct binding energies for many reactions and thus has limited surface chemistry [51]. Combining materials into bimetallic nanostructures is a hot topic because of the possibility to extract a combination of their optical, electronic and catalytic properties.

A core@shell structure is interesting to study because it benefits from the characteristics of the plasmonic core while maintaining a catalytically active surface. The core material should have a lower imaginary part of the dielectric function compared to the shell [52]. This is so that the high energy carriers generated from the decay of the LSPR can preferentially transfer to the shell and enhance catalysis.

Pd is a renowned active catalyst, particularly effective with reactions involving hydrogen and oxygen, however, it does not have excellent or exciting optical properties in the visible region. It absorbs well in the UV with a broad absorption peak at 370 nm because of both its plasmon resonance and interband transitions [53]. Nevertheless, its absorption declines drastically in the visible region, which is not optimal as it reduces the possibility for sunlight driven reactions. By combining a plasmonic core material with a catalytic shell, the decay of the LSPR can be utilized to its maximum by improving selectivity and further enhancing reaction rates while under ambient conditions.

A Au@Pd core@shell (Fig. 2.13) is an optimal design because it allows the Au to act as plasmonic antenna to harvest incoming light while the Pd acts as the catalytic sensitizer at the surface reacting with adsorbates. Pd is suited as the shell material on a Au core as it has a higher imaginary part of the dielectric function compared to Au. Au and Pd have excellent characteristics individually, yet when the metals are put together in a core@shell structure these features couple to form a new construct with hybridized properties.

The first feature, a downfall of the structure, is a damping of the LSPR by the Pd shell through coupling to the Au and interactions with the Pd interband transition.

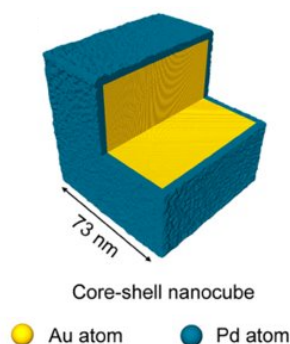


FIGURE 2.13: Au@Pd core@shell nanocube schematic [54]

Since Pd has a high imaginary part of the dielectric function, it is more lossy than Au in the visible range. This is due to the availability of direct interband transitions from the d band to the s band. As previously stated, the consequence of putting these materials together is that the energy should be preferentially dissipated from the gold to the palladium and finally to the adsorbate molecule. This means that the wave is highly damped and the dissipation of energy for free electrons is high. Furthermore, Pd has a larger work function than gold (5.6, 5.3 eV respectively), which means that electrons will flow to the Pd until equilibrium is reached [55]. However, the enhanced near field and hot electron production is damped due to a lowering of hot electrons in Au available [48].

Nevertheless, it has been shown that Au@Pd core@shell structures experience a synergy, even without utilizing the plasmonic properties of Au and using the structures for conventional thermal catalysis [56]. Synergy is when the bimetallic properties are enhanced compared with its mono-metallic counterparts. Figure 2.15 depicts an increase in turn over frequency (TOF) and selectivity with respect to an increasing Pd shell on Au nanorods. The optimal thickness of the Pd shell was found to be 6 atomic layers for maximized thermal catalysis in hydrogenating butadiene. It is difficult to discern exactly the mechanisms which cause the synergy. One explanation owes to the changes induced in both the geometric and electronic properties by having a core@shell structure [57]. Geometrically, there is a lattice constant mismatch between Au (4.079 Å) and Pd (3.8898 Å), and although there is not a very large difference between the two, the small mismatch induces a strain of approximately 4.6% [58]. This lattice strain can cause high adsorption energy of the reactants compared with a single metallic catalyst, which is supported by DFT and has been shown to enhance plasmon driven reactions [56, 59]. If the Pd layer is too thin (<1 nm), the Au core can lower the binding energy of the Pd, which can have a negative impact on catalysis depending on the molecule in question. The lattice strain is high enough to have an effect on catalysis, however it is below 5%, which is the threshold of mismatch for epitaxial growth of

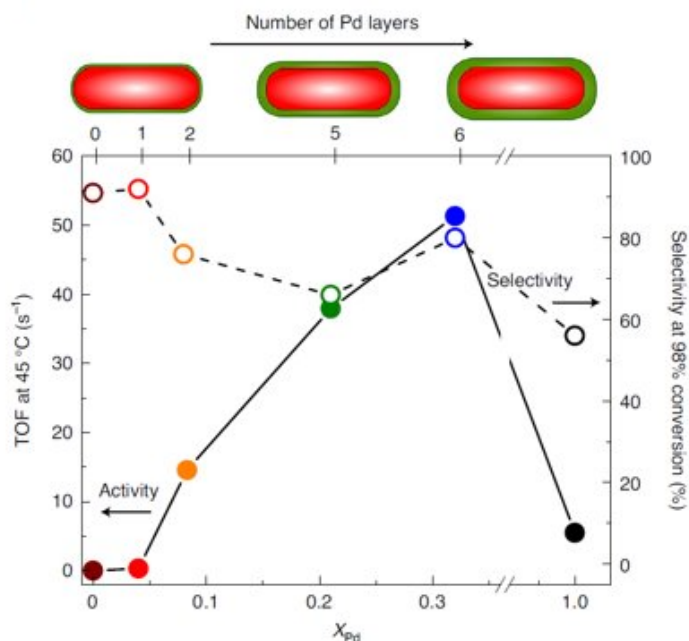


FIGURE 2.14: Synergy of Au@Pd bimetallic nanorods exhibited through conventional thermal catalysis of hydrogenation of butadiene [56]

a metal on another metal [60, 61]. Electronically, combining Au and Pd shifts the d-band orbital overlap of Pd which can affect the shells binding energy through changes in the electronic structure on the surface, which influences the structures interaction with adsorbate molecules. [57, 60, 61].

It has been shown that the properties induced by combining Au@Pd nanoparticles in a core@shell structure also improves plasmon enhanced catalysis. The surface charge heterogeneity due to the LSPR has been identified as be the reason for enhanced catalysis [18, 59]. The surface charge separation on the metals can activate the adsorbed molecule and thus enhance formation of products [59, 62]. Pd is great catalyst for reactions involving hydrogen with Au@Pd core@shells displaying promising results for formic acid dehydrogenation [18]. Formic acid has been proposed as a suitable hydrogen storage material because it is non-toxic and is in a liquid state at room temperature. Furthermore, it has a high density and thus a high volumetric capacity exceeding that of current commercial hydrogen pressure tanks [63]. Using Au nanorods with a thin 2 nm Pd shell on the tips, Zheng et. al saw hydrogen evolution increase almost 15 times under light irradiation compared to in the dark, and even saw results at 5°C comparable to thermal catalysis at 40°C which is shown in Figure 2.14 [18].

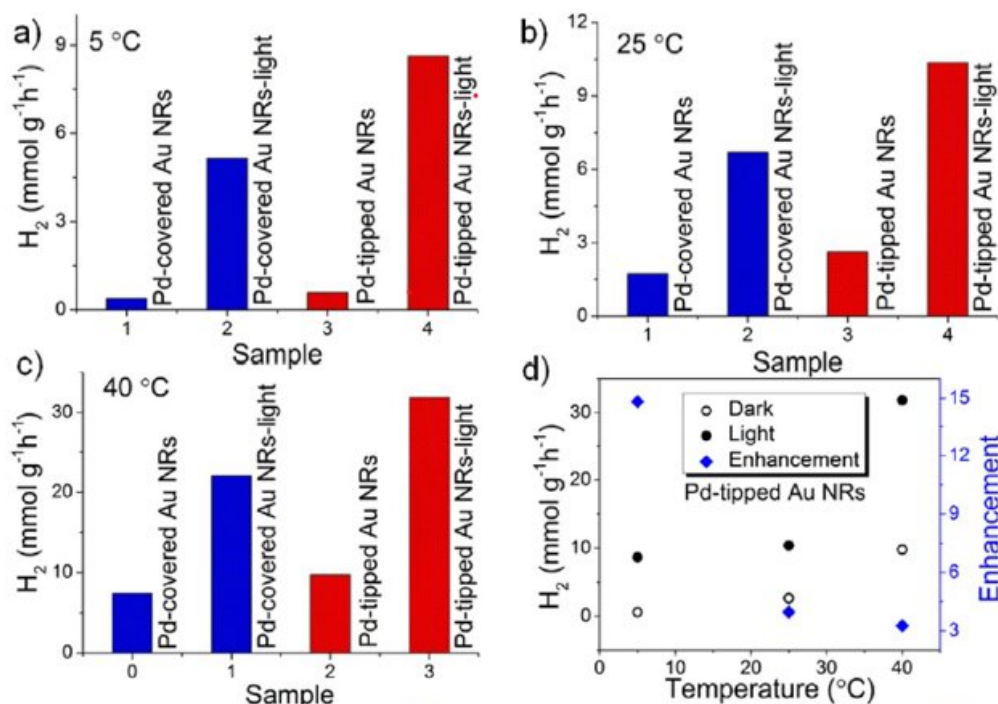
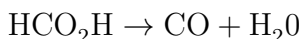
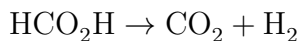


FIGURE 2.15: Plasmon enhanced formic acid dehydrogenation on Pd tipped and Pd covered Au nanorods [18]

Formic acid can undergo two dehydrogenation pathways,



Nonetheless, the group found that the nanostructures selectively dehydrogenated formic acid to CO<sub>2</sub>+H<sub>2</sub>. The CO<sub>2</sub> can then be used as feedstock to produce formic acid, and so the system is carbon neutral. Quenching of photoluminescence was observed at the LSPR which suggests that electrons were transferring to the Pd which induced the surface charge heterogeneity, leading to the enhanced interaction between the Pd and adsorbate. They also conducted a study using platinum as the catalytic shell and saw no enhancement in catalysis. Consequently, they attributed the improved reaction rate on the Au@Pd nanorods to the intrinsic properties of Pd which were improved by the Au core.

Although hydrogen production is critical so that clean energy is available to society, the detection of hydrogen is equally as important. Hydrogen is a colourless, tasteless, odourless gas but is highly flammable [64]. Even at low concentrations, this gas can be a danger to society, with required energy for explosion just 0.017 mJ, an order of magnitude lower than the minimum ignition energy for other flammable gases like

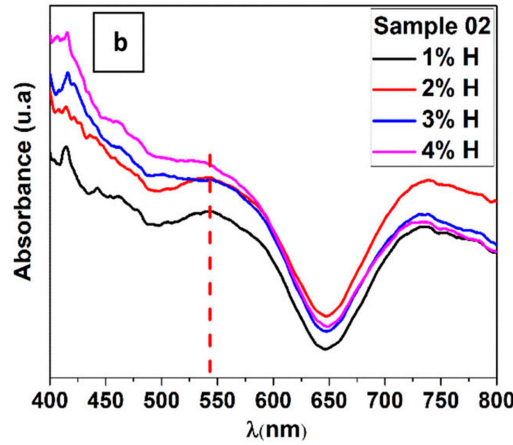
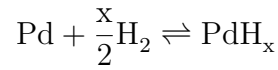


FIGURE 2.16: Absorbance spectra of Au@Pd core@shell nanoparticles on glass substrate with increasing hydrogen concentrations

petrol, butane, methane, ethane and benzene [65]. Au@Pd core@shell nanoparticles are ideal candidates for hydrogen sensing. Figure 2.16 shows the sensitivity of Au@Pd nanoparticles to hydrogen concentration. The Pd shell has a high affinity for absorption of  $H_2$  due to the exothermic and barrier-free dissociative adsorption of  $H_2$  on Pd [51].



A Pd hydride is formed and through the adsorption and desorption of  $H_2$  an  $\alpha$  and  $\beta$  phases generated are detectable using lineshape analysis [64]. This process is reversible which means it is regenerative.

### 2.3.2 Experiment Configuration

Despite reported catalytic enhancements due to the Au@Pd core@shell nanostructures, it is still unclear what is really happening at the interface of the metals. Understanding the effect of the catalytic material on the charge carrier generation from the plasmonic core and how carriers are transferred to the catalytic shell and further to the adsorbate is critical to optimize these systems. Furthermore, the detection limit of optical hydrogen sensors is still below that of electrical sensors [66]. Although utilizing surface lattice resonances has improved the detection limit of optical sensors, a Au@Pd core@shell NCoM has the potential to further enhance the sensitivity.

The following work studies a Au@Pd core@shell NCoM system to explore its ability to be used to track and induce a chemical reaction. This research can be extended to begin to understand processes occurring at the interfaces of the metals. The shape of the particle chosen is a key component in designing this system. It has been found that



anisotropy is favourable for catalysis because it enhances surface charge heterogeneity [18]. For this reason, the nanocube on mirror has been chosen, as it exhibits anisotropy in the NCoM while providing a sharp gap plasmon resonance [38]. The spacer material  $\text{Al}_2\text{O}_3$  is chosen due to its low surface damping and low electron affinity [48]. A Au mirror is used as it is stable has a high reflectivity practically independent of the angle of incidence.

The reactant chosen to study is mercaptobenzoic acid (MBA) (Fig 2.17). MBA forms self assembled monolayers which are required to probe a single molecule on the surface of the nanoparticle and as they make it possible to compare various cubes by assuming a constant surface coverage [67]. Self assembled monolayers also aid in metal-molecule hybridization [50]. Furthermore, MBA has been shown to decarboxylate on plasmonic gold films and nanoparticles resulting in the production of thiophenol (TP) [67–69]. TP has a distinguishable SERS signal compared to MBA therefore the reaction is detectable using this technique. Moreover, it is interesting to see the effect of the Pd shell on this studied reaction mechanism. The catalytic surface combined with the ability to span a wide range of energies due to the NCoM tuneability could unlock new reaction pathways.

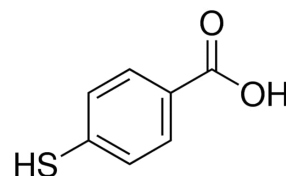


FIGURE 2.17: MBA

## Chapter 3

# Methods

### 3.1 FDTD Simulations

Computational simulations were carried out using the finite-difference-time-domain (FDTD) algorithm from Lumerical Solutions, Inc., which solves Maxwell's Equations. The simulation was run in 3D, with perfectly matched layers (PML) boundary conditions in the  $z$  direction, and anti-symmetric and symmetric boundary conditions in the  $x$  and  $y$  directions respectively. The FDTD simulation region was 500 nm in all directions. The light source used was total-field scattered field with an injection axis along the  $z$  direction and a geometry of 200 nm in all directions. A wavelength range of 250-1200 nm was probed.

The optical constant for Au was taken from values obtained for bulk Au measured by Johnson and Christy [70]. The optical constant for Pd and the  $\text{Al}_2\text{O}_3$  were obtained from Palik [71]. The size of the Au nanocube was initially taken to be 70 nm which was stated by Nanopartz. Once a size distribution of the Au nanocubes was carried out the mean size of the cubes, 65 nm, was used. To imitate the shape of the nanocubes, which in reality have curved corners rather than perfectly sharp corners, the cubes were modelled as a series of rectangles, spheres and circles using the structure group all rounded quadrilaterals located in the extruded polygons tab in the Lumerical software. The radius of the circle, which defines the roundness/sharpness of the corners, was initially taken to be 12 nm. However, upon conducting size distribution calculations the corner radius was taken to be 15 nm and 15.5 nm for Au and Pd respectively. For the NCoM simulations the  $\text{Al}_2\text{O}_3$  layer was placed between a thick Au mirror and the nanocube as shown in Figure 3.1. A detailed mesh of 0.25 nm was placed around the region of interest which covered the gap and went a few nm into the nanocube and the mirror. For the UV-VIS absorption measurement, a single Au-Pd core-shell nanocube in vacuum was simulated.

Absorption and scattering monitors were placed inside and outside of the light source, with geometries of 150 nm and 250 nm in all directions respectively. Data from these monitors was exported to python to calculate extinction cross sections. A 2D

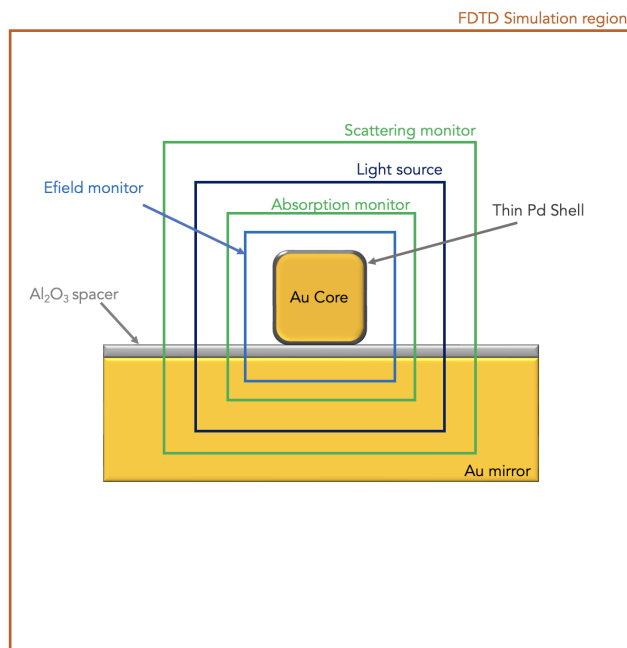


FIGURE 3.1: FDTD Schematic of NCoM simulations

$y$ -normal electric field monitor was placed inside the light source with a geometry of 120 nm in  $x$  and  $z$ , which measured the electric field of the nanocube and in the gap. A refractive index monitor was used to ensure that the program was reading the order of the core and shell correctly. Parameter sweeps were performed using the built in optimizations and sweeps tab. All parameters were defined in the model which were then called in this tab. The data from the sweeps was exported to python and plotted for analysis.

## 3.2 Palladium Shell Overgrowth

### 3.2.1 Chemicals

Gold nanocube colloidal solution (70 nm, citrate capped,  $0.05 \text{ mg mL}^{-1}$ , OD1) was purchased from Nanopartz, Hexadecyltrimethylammonium bromide (CTAB, BioXtra,  $\geq 99\%$ ), Palladium(II) chloride (ReagentPlus  $\text{PdCl}_2$ , 99%), Hydrochloric acid (HCl, ACS Reagent, 37%), L-Ascorbic acid (BioXtra, crystalline,  $\geq 99.0\%$ ), 4-Mercaptobenzoic acid (4-MBA, 99%) were purchased from Sigma-Aldrich.

### 3.2.2 Synthesis

Pd overgrowth on Au nanoparticles has been extensively studied such that the growth mechanism can be tuned by choosing particular parameters. The recipe used in this

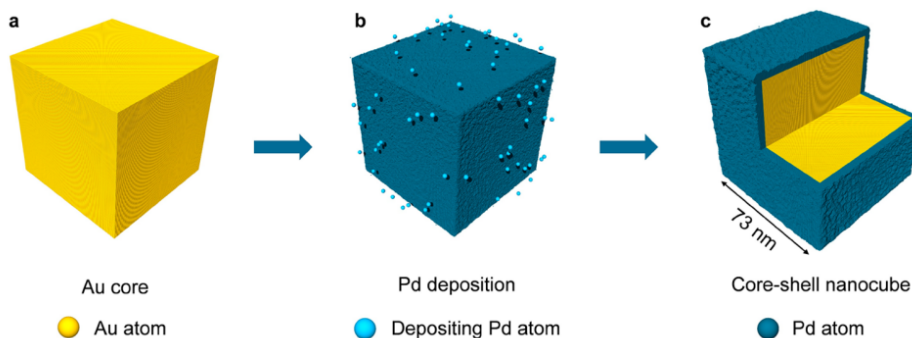


FIGURE 3.2: Au-Pd core-shell nanocube synthesis schematic [54]

work uses the Au nanocubes as the core, the Pd precursor provides the metal ions and the HCl and L-ascorbic acid lightly reduce the ions on the surface of the Au nanocube shown in Figure 3.1. The capping agent CTAB is chosen due the stability it provides. Furthermore, CTAB forms a densely packed bilayer on the surface of the Au nanocube which facilitates epitaxial growth of the Pd, irrespective of their lattice mismatch [72]. Moreover, it has been reported that using CTAB as the capping agent should produce single crystal Pd shell [72].

The protocol by Zheng et al. was followed to make the stock precursor solution, 0.01 M  $\text{H}_2\text{PdCl}_4$  [18]. First, a 0.02 M HCl solution was prepared by slowly adding 0.016 mL HCl to 2.5 mL of deionized water followed by adding 7.5 mL of deionized water. Then, 0.0177 g  $\text{PdCl}_2$  powder was dissolved in the HCl by sonication for 60 minutes at  $60^\circ\text{C}$ .

The procedure for the palladium shell overgrowth was adapted from work by van der Hoeven et al. [56]. A 0.1 M solution of HCl was prepared by slowly adding 0.088 mL HCl to 2.5 mL of deionized water followed by 7.5 mL of deionized water. The precursor solution was diluted to 5.5 mM by combining 1000  $\mu\text{L}$  of the  $\text{H}_2\text{PdCl}_4$  stock solution to 818.2  $\mu\text{L}$  of deionized water. A solution of 22 mM fresh L-ascorbic acid was prepared by adding 0.0387 g L-ascorbic acid to 10 mL Milli-Q water and dissolved via sonication.

A 0.1 M solution of CTAB was prepared by adding 0.1426 g CTAB to 4 mL of deionized water and sonicated until dissolved. In a 7 mL glass vile, which is the reaction vessel, 1 mL of the CTAB solution and 250  $\mu\text{L}$  of the nanocube solution from Nanopartz were added and sonicated for 10 minutes. A magnetic stirrer was added to the vessel and set to stir at 800 rpm. Sequentially, 10  $\mu\text{L}$  of 0.02 M HCl, 10  $\mu\text{L}$   $\text{H}_2\text{PdCl}_4$  and 10  $\mu\text{L}$  of fresh L-ascorbic acid were added to the vessel while stirring at 800 rpm. The solution was left to react for 30 minutes while stirring at 400 rpm. To end the reaction the solution was centrifuged at 4000 rcf for 30 minutes. The supernatant was removed and the nanocubes were redispersed in MilliQ water and washed a further 3

times for purification. The resulting solution was stored at 4°C in the dark.

### 3.2.3 Optical Characterisation

#### UV-VIS Spectroscopy

Steady state absorbance spectra were measured using a LAMBDA 750 UV/Vis/NIR Spectrophotometer (Perkin Elmer). Absorbance spectra were measured from 250-800 nm by using both a deuterium and tungsten lamp to access this wavelength range. The light then passes through a monochromator, so the sample observed the wavelengths sequentially.

The solutions were measured in a quartz cuvette in the spectrophotometer. Quartz was chosen because as it transmits light in the UV-VIS region. When light irradiation hits the solution the sample reflects, scatters, absorbs and transmits light. The wavelength of light absorbed has the required energy to excite an electron from a lower to higher energy level, which produces a characteristic absorbance spectrum [73]. These spectra can be measured using a PbS detector. The absorbance follows a linear relationship at low concentrations according to the Beer-Lambert Law;

$$A = \epsilon dc \quad (3.1)$$

Where  $\epsilon$  is the molar absorptivity in units of  $\text{L mol}^{-1}\text{cm}^{-1}$ ,  $d$  is the path length of light and  $c$  is the concentration. The concentration of the solution should be less than  $\approx 10$  mM. Solutions with a higher concentration behave non-linearly owing to interactions between the analyte and solvent which can induce a different charge distribution in the solution. Since the UV-VIS absorbance spectrum depends on the electronic transitions of the analyte, high concentrations may cause the absorbance wavelengths to shift. Furthermore, at high concentrations the refractive index of the solution may be altered which affects the Beer-Lambert law. To obtain quantitative results the machine should be calibrated with known concentrations of about 5 solutions to obtain a calibration curve. This was not required in this instance since only qualitative results were required.

The absorbance spectrum of MilliQ water was measured as the reference. This was followed by measuring the absorbance spectrum of the bare Au nanocubes (nanocubes before overgrowth) by adding 250  $\mu\text{L}$  of the Nanopartz Au nanocubes to 1 mL of MilliQ water. Subsequently, the absorbance spectrum of the nanocube solution after overgrowth was measured. The data was exported to python where the reference was subtracted from the absorbance spectra of the nanocube solutions to obtain the absorbance of the nanocubes.

### 3.2.4 Elemental Characterisation

#### Transmission Electron Microscope - Energy Dispersive X-Ray Spectroscopy (TEM-EDS)

A Spectra 30-300kV (S)TEM was used for initial elemental characterisation of the nanocubes after Pd shell overgrowth. It is a double aberration corrected electron microscope which was operated by dr. Ali Kosari at the Electron Microscopy Centre, Utrecht University. The microscope was operated at 300 keV. The nanocube solution after overgrowth was sonicated for 15 minutes prior to dropcasting 8  $\mu$ L of the solution on a carbon film coated carbon supported copper TEM grid. The droplet was allowed to dry in air at room temperature. This process was repeated once to ensure an adequate concentration of particles were on the TEM grid. The sample was loaded in a double-tilt TEM holder and plasma cleaned for 2 seconds to remove contaminants. The Spectra 30-300kV (S)TEM is equipped with a SuperX detection system for Energy-Dispersive X-ray Spectroscopy (EDS) which was used for the elemental mapping of the Au@Pd core@shell nanocubes.

Bright field STEM operates by shooting electrons at a sample and collecting the transmitted electrons. This is carried out under vacuum to ensure that molecules present in the machine do not interact with the electron beam. Electromagnetic lenses focus the electrons in a narrow beam. Some electrons will be scattered by the specimen depending on its composition and orientation. These electrons are detected, and an image is formed. For the EDS measurements, a beam of high energy electrons is shot at the sample. This ionizes the atoms in the sample and removes electrons from the inner atomic shells. Higher energy outer shell electrons then fall into the holes created and release energy in the form of X-rays. An X-ray detector collects the signals and due to the principle that every element has a unique atomic structure, therefore the process leaves an atomic fingerprint enabling the identification of the elements.

#### Scanning Electron Microscope - Energy Dispersive X-Ray Spectroscopy (SEM-EDS)

Further elemental data on the same sample (on TEM grid) was obtained using an FEI Verios 460, a high-resolution Scanning Electron Microscope (SEM) equipped with an Oxford EDS detector which was operated at 15 kV and 1 nA. Conducting measurements on the TEM grids enabled higher signal acquisition due to less noise from scattering that would occur on a silicon substrate. Elemental linescans of the Au@Pd core@shell nanocubes were conducted to obtain linescan data and EDS elemental spectra. In an SEM, back-scattered electrons are detected, compared with transmitted electrons which are detected in a TEM. In a similar set-up to TEM, under vacuum, an electron

beam passes through numerous electromagnetic lenses and is directed at the sample. To obtain high resolution images immersion mode was used to image the nanoparticles. In this mode, the sample is in a magnetic field so that secondary electrons are detected. These electrons come from atoms in the sample and are inelastic due to the loss of energy from the primary electron and provide information about the surface of the specimen. The SEM-EDS detector operates in the same way as the TEM-EDS detector. The resulting spectrum obtained is intensity vs. X-ray energy. The Oxford Aztec software performed tricks to help identify what elements correspond to the observed peaks.

### 3.2.5 Structural Characterisation

#### High Angle Annular Dark Field - Scanning Transmission Electron Microscopy (HAADF-STEM)

The structure of the Au@Pd core@shell nanocubes was investigated with the Spectra 30-300kV (S)TEM. The same sample was used as in the elemental characterisation. Images were taken in dark field mode which is where the beam that passes through the objective aperture is centred on a diffraction point. This means that only electrons which are diffracted by crystalline specimen in on the substrate are collected. An annular dark field detector is placed at high angles with respect to the diffracted beam. This is to avoid Bragg diffracted electrons and only detect high angle incoherently scattered (Rutherford scattered) electrons [74]. The angle that these electrons are scattered by ( $\theta$ ) is highly dependent on the material weight i.e., the atomic number  $Z$ . Therefore, the core and shell can be identified due to the difference in  $Z$  contrast. Since Pd has a lower atomic number than Au it will show up darker compared with Au.

#### High Resolution Transmission Electron Microscopy (HRTEM)

The Spectra 30-300kV (S)TEM was used for high resolution TEM imaging to identify the lattice matching of the Au@Pd core@shell structures. This is bright field TEM imaging with a resolution high enough to identify lattice spacings. The resolution is improved by using both transmitted and scattered beams which create an interference image. The same sample as for TEM-EDS and HAADF-STEM was used.

#### Particle Size Distribution

The average size of Au core nanoparticles prior to Pd shell overgrowth was measured using the FEI Verios operated at 5 kV and 100 pA. The data was imported to the

software package ImageJ and the size of 100 Au nanocubes was measured. The acquired data was used for further simulations.

## 3.3 Nanocavity Fabrication

### 3.3.1 Chemicals

Ammonia ( $\text{NH}_4\text{OH}$  30%), Hydrogen Peroxide ( $\text{H}_2\text{O}_2$  30%), Trimethylaluminium ( $\text{Al}_2(\text{CH}_3)_6$ , 97%) were purchased from Sigma Aldrich. Negative resist (ma-N 1420) was purchased from Micro Resist Technology GmbH, Hexamethyldisilazane (HDMS), UV-Lithography developer (Ma-D 533s), MilliQ  $\text{H}_2\text{O}$ , Samples were prepared on silicon  $\langle 100 \rangle$  substrates.

### 3.3.2 Substrate Preparation

#### Base Piranha

The silicon substrates were sonicated for 15 minutes sequentially in deionized water, acetone and isopropanol to remove the resist layer which was used to protect the wafers when they were being cut. This procedure was followed by a standard base piranha clean, a 5:1:1 mixture of  $\text{H}_2\text{O} : \text{NH}_4\text{OH} : \text{H}_2\text{O}_2$ . The substrates were first sonicated in deionized water. Then a beaker was filled with 5 parts deionized water and heated to  $75^\circ\text{C}$ . Then, 1 part  $\text{NH}_4\text{OH}$  was added while the solution was stirred by magnetic stirrer. Once the solution returned to  $75^\circ\text{C}$ , 1 part  $\text{H}_2\text{O}_2$  was added. The silicon substrates were then added to the base piranha solution and left for 15 minutes. The samples were removed, washed with water and isopropanol, and dried with an  $\text{N}_2$  gun.

#### Plasma Cleaning

To remove any remaining contaminants the substrates received mild oxygen plasma descumming (Diener Electronic Pico QR-200-PCCE) for 2 minutes. Oxygen gas was introduced in the plasma chamber and was converted to plasma using high frequency voltages at low pressure.

### 3.3.3 Fabrication

#### Spin Coating

Prior to UV-Lithography, a photoresist was spin coated on the substrates. Spin coating is a method of forming thin films on substrates. The substrate is placed in the spin-coater and a drop of the desired film material is dropcasted on the substrate. Assuming the drop covers the entire substrate, the volume dropcasted does not determine film



thickness. The film thickness depends on the viscosity of the solution and the settings chosen in the spin coater.

An adhesion promoting layer of HDMS was spincoated on the substrates (Suss MicroTec-Delta 80) with a ramp speed of  $1000 \text{ rpm s}^{-1}$  and a spin speed of 4000 rpm for 35 s. The substrates were then baked at  $150^\circ\text{C}$  for 60 s. Following the adhesion layer, the negative photoresist ma-N 1420 was spincoated on the substrates with a ramp speed of  $1000 \text{ rpm s}^{-1}$  and a spin speed of 4000 rpm for 45 s. The substrates were then baked at  $120^\circ\text{C}$  for 120 s. The thickness of the resist was measured using the KLA Tencor Stylus Profiler P7.

### UV-Lithography

The substrates were patterned by UV-lithography (Suss MABA6, UV Mask aligner). Using an optical mask, a pattern can be imprinted on the substrate. UV light is used to transfer the design of the mask to the photoresist which was spin coated on the substrate prior to UV-Exposure.

The substrates were exposed to UV for 12 s at  $25 \text{ mWcm}^{-2}$  through the photolithography mask comprised of labelled grids with numbered squares of  $100 \mu\text{m}^2$ . A negative resist was used which means that it was strengthened under UV illumination. The pattern was developed by immersing the substrates in Ma-D 533s for 90 s which dissolved the resist in the regions which were not exposed to UV.

### Thermal Evaporation

A 5 nm chromium adhesion layer followed by a 100 nm gold layer were evaporated on the substrates using an AMOLF home built thermal evaporator (Nanoontje). The material pellets were placed in tungsten boats and evaporated by passing an electrical current through the boat. The deposition rate was maintained  $0.05 \text{ nms}^{-1}$  by adjusting the current which controls evaporation rate and thus the deposition rate.

### Lift-Off

The substrates were soaked in acetone for 1 hour followed by 5 minutes of syringing to lift-off the resist. Since a negative resist was used and any resist in the fields was previously removed, only the grid lines and numbers were lifted off. Leaving behind gold fields encompassed by silicon grid lines and silicon numbers.

### Atomic Layer Deposition (ALD)

An AMOLF home built atomic layer deposition (ALD) system was used to deposit the thin layers of  $\text{Al}_2\text{O}_3$  on the gold mirrors. In ALD, vaporised precursors are added

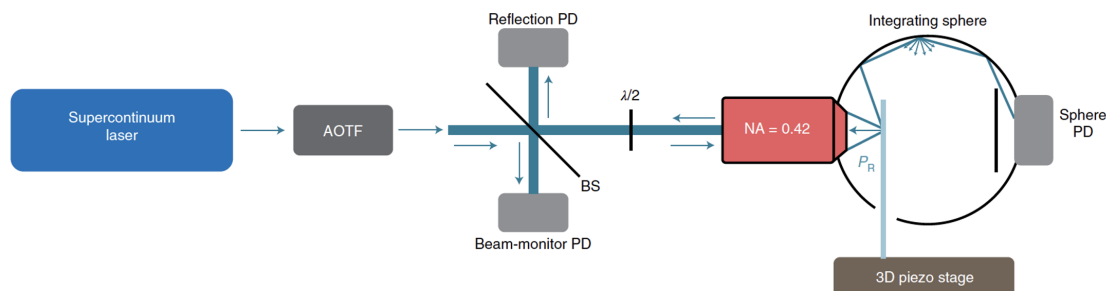


FIGURE 3.3: Optical set up schematic [38]

sequentially. Each precursor reacts with the substrate surface in a self limiting way so that the reaction ends when all reactive sites of the substrate are used [75]. The pressure of the system was maintained at 1.1 mbar and the stage was set to 250°C. The system was first conditioned (run without substrates) for 50 cycles of 20 ms MilliQ H<sub>2</sub>O, 20000 ms delay, 20 ms Al<sub>2</sub>(CH<sub>3</sub>)<sub>6</sub> and 20000 ms delay. The delay time was to allow the precursor time to react with the surface. The thickness of the Al<sub>2</sub>O<sub>3</sub> layer was determined by the number of cycles performed, with each 10 cycles amounting to 1.2 nm of Al<sub>2</sub>O<sub>3</sub>. Two substrates of 10, 20, 50 cycles each were ran.

## Dropcasting

Finally, the nanocavities were formed by dropcasting the nanocube solutions on the desired grid on the Al<sub>2</sub>O<sub>3</sub> and Au mirror. First, the Au and Au@Pd nanocube solutions were sonicated for 15 minutes. Bare Au nanocavities were fabricated by dropcasting 10  $\mu$ L Au nanocubes for 10 minutes followed by washing with deionized water. This process was repeated to ensure an adequate concentration of Au particles on the grid. The Au@Pd nanocavities were formed by dropcasting 10  $\mu$ L of the nanocube solution on the desired grid for 10 minutes followed by another 10  $\mu$ L drop and let to dry in air at room temperature. The samples were then soaked in ethanol for 24 hours to remove any residue and were dried with an N<sub>2</sub> gun.

## 3.3.4 Characterisation

### Integrating Sphere Spectroscopy

The nanocavities were characterised using an integrating sphere spectroscopy setup shown in Figure 3.3. A supercontinuum laser (NKT Photonics, SuperK FIANIUM) is used to enable access to a broad range of wavelengths (390 – 2400 nm). The broad light source is sent through an acousto-optic tunable filter (AOTF, Crystal Technologies) so that specific wavelengths can be chosen. The beam then passes through a polarizing beam splitter which allows only one polarization of light through (Thorlabs). Neutral

density filters (Thorlabs) are included to enable simple control of the intensity of the beam hitting the sample. Then, the beam passes through a beam splitter directing half of the light to photodetector (M) which acts as a beam monitor to account for fluctuations in laser intensity. The rest of the light is directed through an objective (Mitutoyo M ApoPlan NIR  $\times 50$ ) with an NA= 0.42, where it is focused on the sample which is placed on a 3D piezo stage (Piezajena Tritor400) inside an integrating sphere (LabSphere, GPS-020-SL). A photodetector (IS) is placed behind the integrating sphere which collects the scattered light, while the reflected light passes back through the objective to the beam splitter, where it is directed to the third photodetector (R). The three photodetectors are connected to Stanford Research Systems SR830 lock-in amplifiers which receive the lock-in from the AOTF to improve the signal. The set up is equipped with a CCD camera (Thorlabs) and a white light source so that location in the sample is known using optical microscopy to locate the field of interest.

Spatially resolved extinction spectra were obtained by scanning over a large area of interest in steps of 1  $\mu\text{m}$ . These fields were first chosen by first taking high-resolution SEM images using the FEI Verios 460 at 5 kV acceleration voltage and 100 pA. Low magnification (8000x) images of the fields were taken at a high scan resolution (6144x4096) pixels and a dwell time of 3  $\mu\text{s}$ . This method provides the ability to image a large area, while maintaining the capacity to identify nanocubes by zooming in on the suspected cube. These low magnification, high resolution SEM images were overlaid with the large area extinction maps. A dip in reflection in the extinction map suggested that a nanocube was present since the substrate is a mirror and should have almost perfect reflectance. When a pixel was identified as a prospective nanocube, it was cross checked with the SEM image shown in Figure 3.4 a. If the structure was identified to be a nanocube, a high resolution 0.5  $\mu\text{m}$  extinction map was taken in the region of the nanocube to identify the exact pixel of the cube. The nanocube was then characterised by conducting a full wavelength scan on it and recording the resulting extinction spectrum.

Extinction describes the amount of energy removed from the light beam where;

$$P_{ext} = P_{abs} + P_{scat} \quad (3.2)$$

Where  $P_{abs}$  is the power absorbed and  $P_{scat}$  is the power scattered. The power incident on the sample is;

$$P_{in} = P_{ref} + P_{abs} + P_{sca} \quad (3.3)$$

Where  $P_{ref}$  is the power reflected. Now,

$$P_{abs} + P_{sca} = P_{in} - P_{ref} \quad (3.4)$$

Subbing equation 3.4 in to equation 3.2 gives,

$$P_{ext} = P_{in} - P_{ref} \quad (3.5)$$

Dividing through by  $P_{in}$  gives unitless extinction,

$$Extinction = 1 - R \quad (3.6)$$

Three measurements were taken for each wavelength and averaged to give one extinction value in steps of 2.5 nm. The spectra were analysed in python by conducting a Lorentzian fit on the gap plasmon resonance to extract the full width half max (FWHM), resonant energy ( $E_{res}$ ), and thus the Q factor.

### Cathodoluminescence (CL)

Cathodoluminescence (CL) describes light that is generated by electrons in a cathode ray. When the cathode ray, which is a beam of high-energy electrons, hits the specimen most of the energy is absorbed generating phonons. However, some of the energy is converted to X-rays, secondary electrons, Auger electrons and photons which is known as CL [76]. The electron beam acts as a broadband light source, exciting all plasmon modes at once. Coherent CL is where the electron beam polarizes the material generating an oscillating charge inducing the emission of a photon which is related to the polarization of the material, which dominates for plasmon modes. Incoherent CL is similar to photoluminescence but the cathode ray carries more energy and quanta than light [77]. Interband transitions lead to incoherent radiation. The spatial variation of the plasmon modes can be identified by looking at variation of photon emission in a CL map [78].

Cathodoluminescence measurements were taken in a modified Thermo Fisher Quanta 650 SEM equipped with a Schottky field emission gun (FEG) capable of generating electrons from a few 100s eV to 30 keV. The electrons were shot at the sample through 600  $\mu\text{m}$  hole in a parabolic mirror with an acceleration voltage of 20 keV. This mirror also collected the emitted light from the sample which was directed through a series of optical instruments and coupled to a silicon charge coupled device array detector.

## 3.4 Plasmon Driven Reaction on a Single Nanocavity

### 3.4.1 Ligand Exchange

The ligand exchange was carried out by first dissolving 0.0463 g of MBA in 20 mL of ethanol to give a 15 mM solution of ethanoic MBA. The substrates with the nanocavities were immersed the MBA for 16 hours, followed by 3 hours in ethanol. They were then dried using an N<sub>2</sub> gun.

### 3.4.2 Lineshape Analysis

Plasmon driven reactions on the surface of a single nanocube were tracked and induced by conducting 10 consecutive wavelength scans from 500-780 nm on a nanocavity. The nanocavities were located and measured using the integrating sphere set up and with same procedure as for the cavity characterisation (3.3.4) and shown in Figure 3.4 a. Changes induced by each wavelength scan to the FWHM and resonant energy were

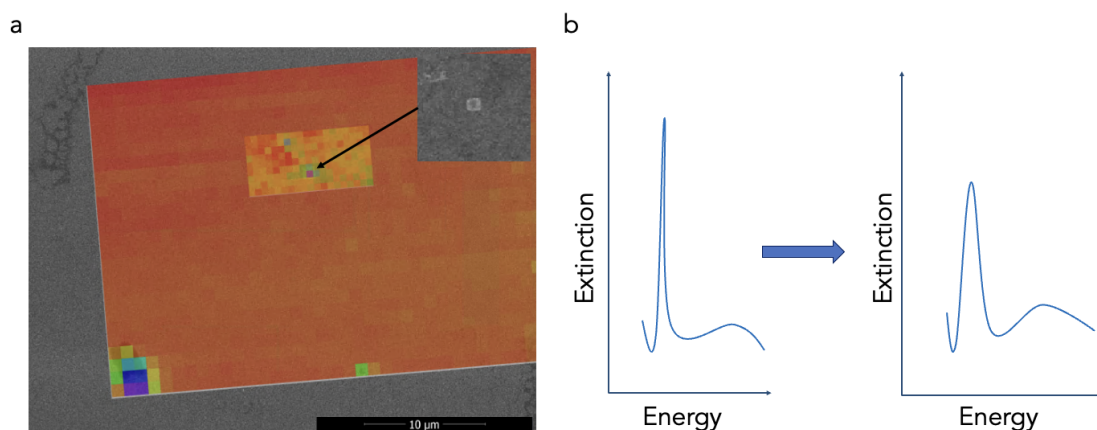


FIGURE 3.4: (a) Overlay of high resolution, low magnification image with extinction map to identify nanocube for extinction measurement. (b) Schematic of change of lineshape from first to tenth wavelength scan

tracked and analysed to understand what was happening at the surface of the nanocube (Fig 3.4 b).

## Chapter 4

# Results and Discussion

### 4.1 FDTD Simulations

#### 4.1.1 UV-VIS Spectroscopy Simulations

The first step in realizing the Au@Pd NCoMs is to obtain colloidal solution of Au@Pd core@shell nanocubes by growing a thin Pd shell on 70 nm Au nanocubes. A UV-VIS spectroscopy simulation was used to get qualitative information of what the UV-VIS absorbance results should look like before and after the Pd shell overgrowth. The simulation was performed on a single nanocube in vacuum. Hence, the simulation was not expected to match perfectly with the experimentally obtained UV-VIS spectra since the measured spectra are taken of an ensemble of colloidal nanoparticles in water. Furthermore, the simulation yields the absorption cross section, and the UV-VIS spectra are measured as absorbance. Nevertheless, from Figure 4.1 it can be deduced that Pd

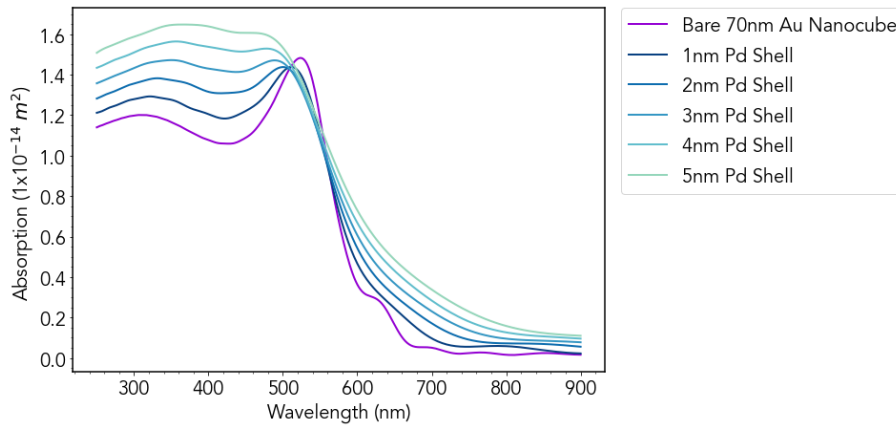


FIGURE 4.1: UV-VIS Absorption simulation of single a Au@Pd core@shell nanocube in vacuum

shell growth on the Au nanocubes should maintain the Au LSPR peak but will broaden and blue shift the peak according to how thick the shell is. For a thick Pd shell, ( $> 4$  nm), the Au LSPR peak is smeared across the UV-VIS region (250-500 nm). Since a thin Pd shell is desired, an absorbance peak should be present at the Au nanocube

resonant energy at  $\approx 550$  nm but should be blue shifted by  $\approx 20$  nm and broadened by  $\approx 10$  nm according to the simulation.

### 4.1.2 Effect of Pd Shell Thickness in NCoM

Simulations of the Au@Pd core@shell NCoM were run to understand the screening that the Pd shell has on the Au plasmonic core and its effect on the gap plasmon resonance shown in Figure 4.2. The gap mode is seen between 750 and 850 nm. This

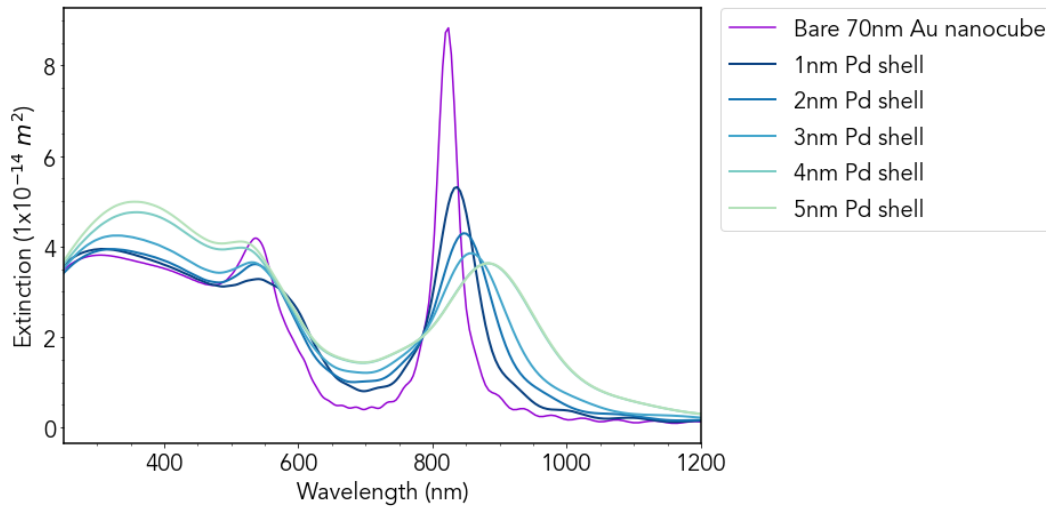


FIGURE 4.2: Simulation of extinction of Au and Au@Pd core@shell NCoM with increasing Pd shell thickness (5 nm spacer). The gap plasmon resonances lie between 750-950 nm

mode is called the gap mode because it is not seen for Au or Au@Pd nanoparticles outside of the NCoM and is vocalized in the gap. The second order mode, named the antenna mode, is at about 550 nm. As mentioned in section 2.2.3, these modes cannot be completely deconvoluted as they are a hybridization of the plasmonic nanocube and nanoscale Fabry-Perot modes but are named in this manner for ease of discussion.

Interestingly, in the region of the Au interband transitions (450-600 nm), increasing the thickness of the Pd shell induces a broadened blue shift and an increase in extinction. As discussed in 2.3.1, Pd absorbs strongly and broadly in the UV region, which explains the behaviour of the extinction spectra in the interband regime.

The gap mode also shows a broadening but a contrasting a red shift and decrease of the extinction as the shell thickness increases. The damping of the gap plasmon resonance is expected, since the Pd has a higher value for the imaginary part of the dielectric function than Au and is therefore more lossy than Au as mentioned in 2.3.1. The red shift in plasmon resonance can be explained by looking at the refractive index difference of the metals. According to Johnson and Christy, Au has a refractive index of 0.28 which is smaller than for Pd which is 1.69 [70]. The increased refractive

index in Pd compared with Au means that a lower energy is required to excite the collective oscillation of the conduction band electrons [79]. This is because materials with a higher refractive index also have a higher dielectric function. Due to the higher dielectric function, there will be greater polarization of the Pd which attenuates the accumulating charge. This attenuation reduces the restoring force which reduces the resonant frequency and thus increases the resonant wavelength.

To understand the effect of the NCoM construct on the field enhancement, a simulation of an Au@Pd core@shell nanocube was simulated in Figure 4.3 with (a) an Au@Pd nanoparticle and (b) Au@Pd NCoM. The colour bar indicates the field enhancement

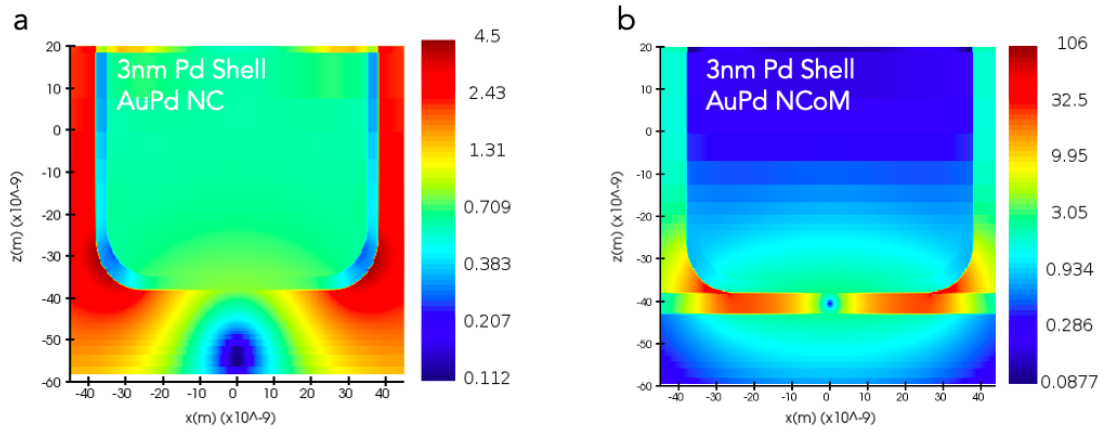


FIGURE 4.3: Simulation of electric field enhancement of (a) Au@Pd core@shell Nanocube and (b) Au@Pd NCoM for a 3 nm Pd shell (5 nm spacer). The colour bar represents the enhancement factor  $|E/E_0|$

factor  $|E/E_0|$ , with the maximum enhancement for the Au@Pd nanocube at the corners of the cube of 4.5. The maximum field enhancement for the Au@Pd NCoM is 106, which is visible on the corners of the cube and in the gap. The NCoM induces an electric field enhancement an order of magnitude higher than a single nanocube, translating to two orders of magnitude for the magnitude for the intensity enhancement  $|E/E_0|^2$ .

Furthermore, it is important to consider the impact of the Pd shell on the field enhancement in the gap which is shown in Figure 4.4. Although the enhancement decreases as the Pd shell thickness increases, it still exhibits a significant enhancement of about an order of magnitude even for a 5 nm Pd shell.

These simulations provide key information that will carry through to the rest of the project, firstly that a Au@Pd core@shell nanocube can exhibit a gap plasmon resonance in an NCoM, and secondly that the Pd shell must be thin to maintain the shape and intensity of the Lorentzian of the gap resonance and further to sustain extreme enhanced fields.



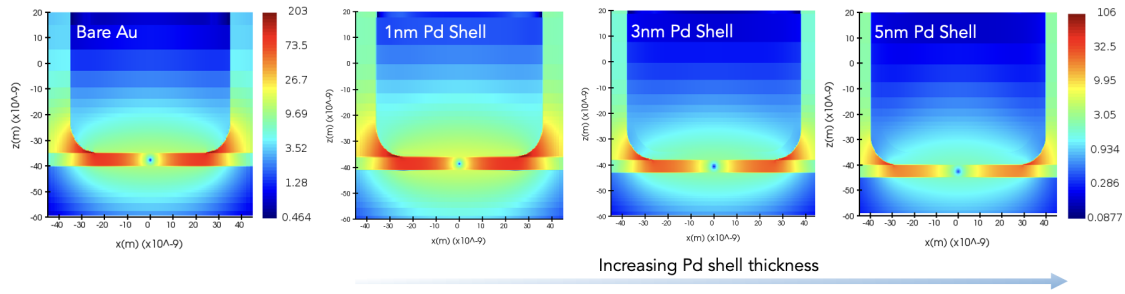


FIGURE 4.4: Simulation of electric field enhancement of Au and Au@Pd core@shell NCoM with increasing Pd shell thickness (5 nm spacer)

### 4.1.3 Effect of Dielectric Spacer Thickness in NCoM

It is now established that a thin Pd shell is desired for experiments, and for this reason a 3 nm Pd shell is used to study the effect of spacer thickness in the NCoM.

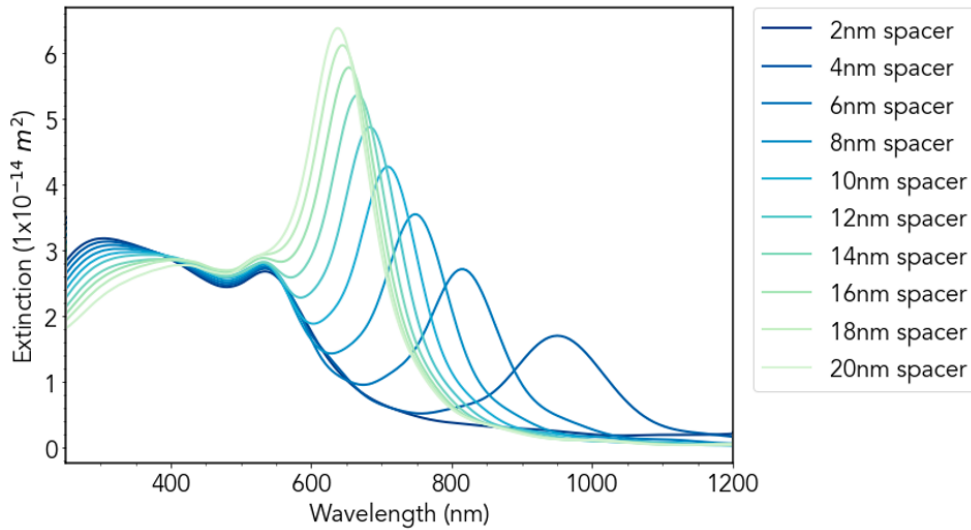


FIGURE 4.5: Simulation of extinction of Au@Pd core@shell NCoM with increasing dielectric spacer thickness (70 nm Au, 3 nm Pd shell)

Increasing the spacer thickness induces a significant blue shift and narrowing of the gap resonance. As discussed in section 2.2.3, this is attributed to the reduction in coupling strength of the cavity to the electric field. Once the gap thickness is  $>10$  nm the gap mode couples with the antenna mode. This is not advantageous as it makes it difficult to excite just the gap mode and avoid the Au interband transitions. Furthermore, disentangling chemical processes produced by interband electrons or plasmon produced hot electrons becomes difficult. Therefore, spacers  $>10$  nm are unfavourable for gap mode lineshape analysis.

#### 4.1.4 Effect of Gold Core Dimensions in NCoM

Another important aspect to consider is that colloidal solutions of nanoparticles have a size dispersity. The Au nanocubes used in this work are from Nanopartz, who state that the standard deviation of the cubes is 5%, however from a brief look at the particles in the SEM it was apparent that the size distribution is larger. The simulation in Figure 4.6 shows the Au@Pd NCoM with increasing Au core dimensions, while the Pd shell is fixed at 3 nm and the spacer set to 5 nm.

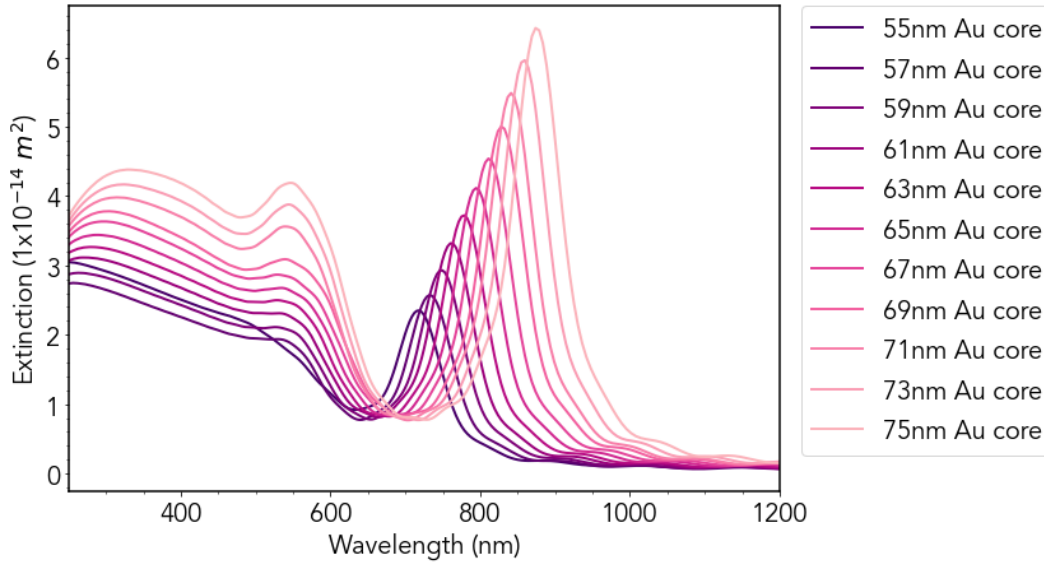


FIGURE 4.6: Simulation of extinction of Au NCoM with increasing core size (2 nm Pd shell, 5 nm spacer)

As the core size increases, the resonant wavelength of the gap mode is red shifted and increases in magnitude significantly. This could be since a larger core results in the 'good' plasmonic to 'poor' plasmonic material ratio increasing as the core size increases and the shell thickness is constant. This allows for stronger coupling between the cavity and the electric field due to the stronger dipole interactions because of the increased ratio. Changes in the antenna mode are not as obvious. There is not a notable change in the resonant wavelength, however the Au LSPR becomes much more pronounced as the core becomes larger. Again, this could be due to the ratio of Au to the Pd increasing significantly.

## 4.2 Pd Shell Overgrowth

### 4.2.1 Optical Characterisation

The measured and simulated UV-VIS absorbance spectra are shown in Figure 4.7. Qualitatively, in both simulation and experiment the spectrum after the shell growth

maintains a peak around the Au LSPR. Moreover, in both simulation and experiment the spectrum is broadened, however in experiment the blue shift is not observed. The simulation and experimental conditions were different, as the simulation was of a single particle without a solvent as described in 4.1.1, which explains the discrepancy. Nev-

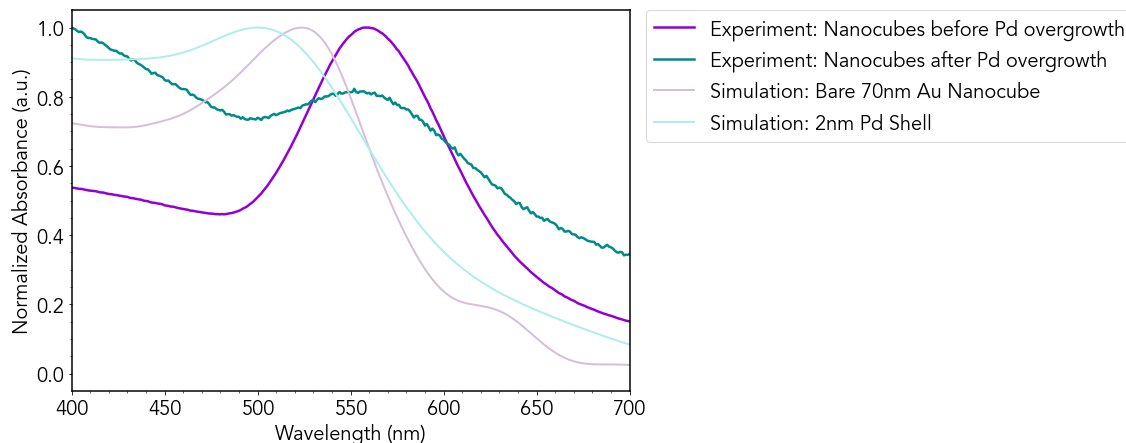


FIGURE 4.7: Normalized measured and simulated UV-VIS absorbance before and after Pd shell overgrowth

ertheless, this sample produced a broadened Au LSPR peak which suggested that a thin Pd shell had been formed. The signal was weak for the solution after overgrowth, which suggested that a low concentration of particles was obtained. This is due to the loss of particles during the numerous purification steps taken at the end of the synthesis to remove residual CTAB.

## 4.2.2 Elemental Characterisation

The elemental maps taken in the EDS-TEM in Utrecht are shown in Figure 4.8. There

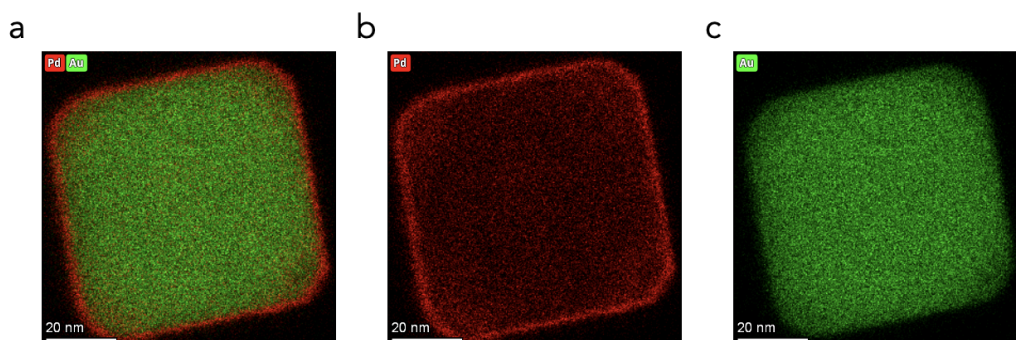


FIGURE 4.8: TEM-EDS Measurement of Au@Pd core@shell nanocube by Ali Kosari

is clearly a thin Pd shell on the surface which can be seen in red in Figure 4.8 b. The

Pd signal is much stronger on the surface than in the core indicating that it is indeed an Au@Pd core@shell nanocube.

Further elemental analysis was carried out using a SEM-EDS system. A linescan was drawn through the center of a nanocube which can be seen in Figure 4.9a. The

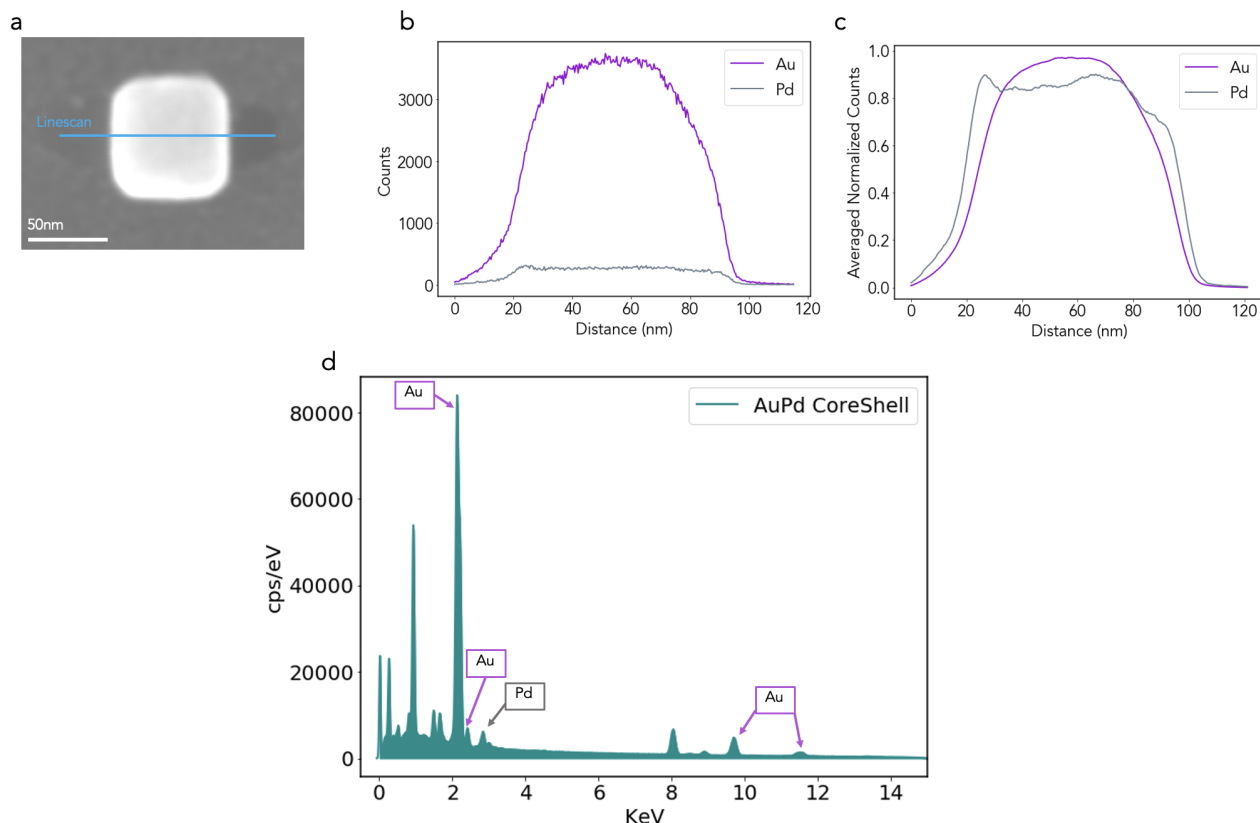


FIGURE 4.9: a. SEM-EDS data linescan on Au@Pd nanocube shown b. linescan plot, c. normalized smoothened linescan plot, d. EDS spectrum

core@shell structure can be identified through analysis of the linescan (Fig. 4.9a,b,c). These figures depict the same data; however c is a normalized and smoothed version. This is to clearly show how the shell can be identified by the shape of the Pd curve with respect to the Au. The Pd has peaks on the edges which are due the shell providing a higher Pd signal because Au is not present in this region. The linescan data is accompanied by an EDS spectrum (Fig 4.9d) which further confirms that Au@Pd nanoparticles have been obtained.

### 4.2.3 Structural Characterisation

The HRTEM image shown in Figure 4.10 a depicts a continuous fringe pattern through the entire particle suggesting the lattice matching of the core and shell [80]. Furthermore, this is evidence of epitaxial growth of the Pd shell. In HAADF-STEM mode the core and shell could be identified through differences in the Z contrast. As anticipated,

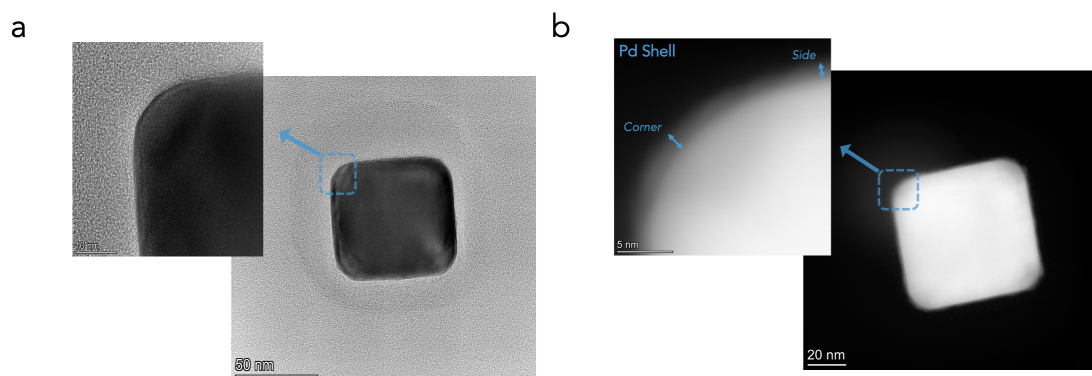


FIGURE 4.10: a. High resolution TEM image of Au@Pd nanocube showing continuous lattice fringes, b. HAADF-STEM image of Au@Pd nanocube showing Pd shell due to Z contrast

the Pd shell shows lower contrast compared to the bright white Au core shown in Figure 4.10 b. In initial imaging it became clear that corners of the shells were thicker than the sides. Furthermore, the thickness of the shell was non uniform from corner to corner and side to side. For these reasons a measurement for each corner and each side was taken for 36 cubes to obtain an average corner and side thickness for each cube. The shell thickness distribution is displayed in Figure 4.11. Despite the thickness

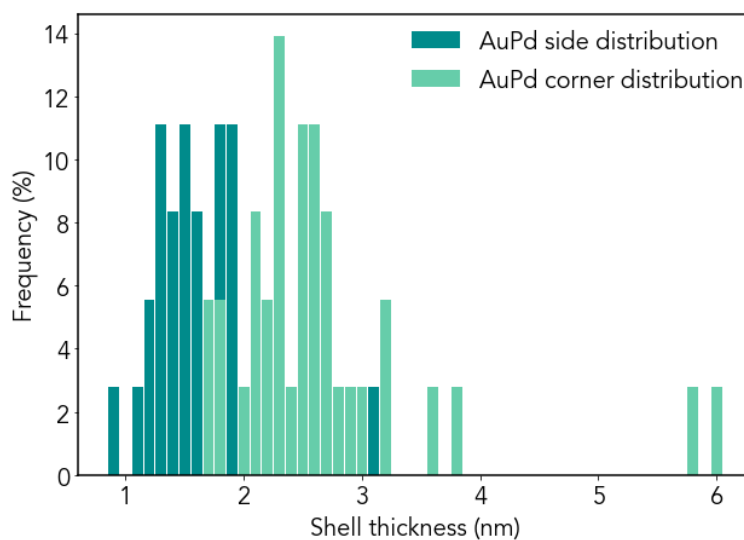


FIGURE 4.11: Bar chart of frequency percent versus shell dimension for both corner thickness and side thickness obtained from HAADF-STEM imaging of Au@Pd core@shell nanocubes

dispersity, in general the shell thickness is in the realm of what is desired to optimize the trade-off between the plasmon screening and required thickness for the Pd shell to enhance catalysis, which is between 1 and 3 nm. The mean corner thickness obtained is  $2.68 \pm 0.911$  nm and the average side thickness is  $1.75 \pm 0.582$  nm. Furthermore, a

size distribution analysis was carried out on the Au nanocubes prior to Pd overgrowth. The mean size of the Au nanocube obtained is  $65 \pm 3.3\text{nm}$ . The data obtained from

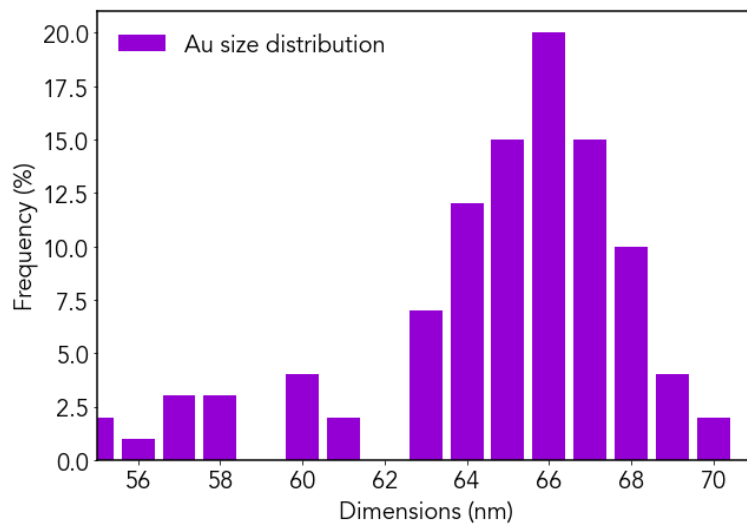


FIGURE 4.12: Bar chart of frequency percent of core side dimension obtained from SEM images of Au nanoparticles and calculated in ImageJ

the size distribution analysis was input to the FDTD simulations for more accurate simulations. The simulation for the Au@Pd core@shell NCoM with the experimental data input is shown in Figure 4.13 for an increasing spacer thickness.

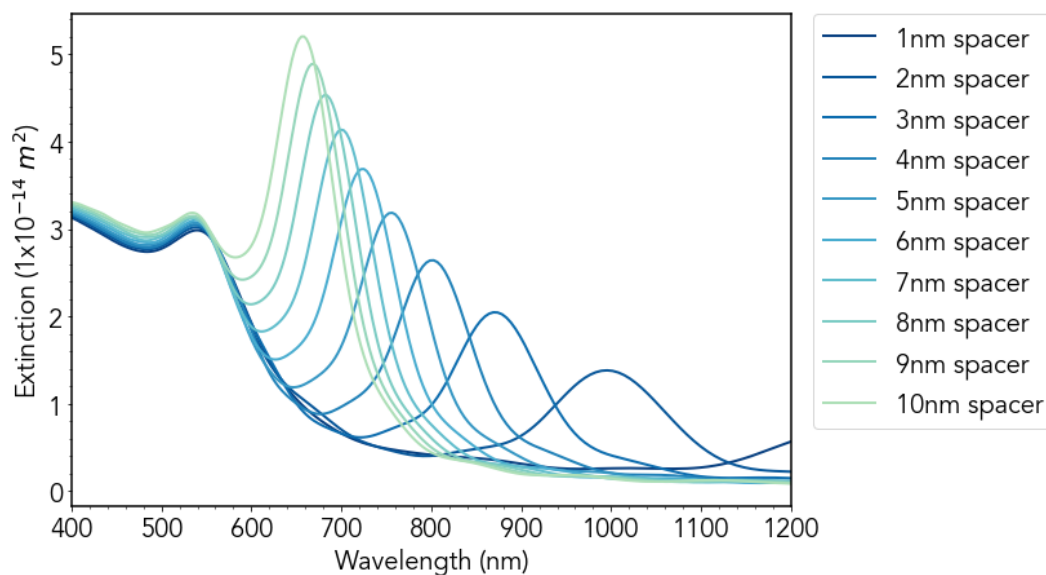


FIGURE 4.13: Simulation of extinction of Au@Pd core@shell with size data input NCoM with increasing dielectric spacer thickness



## 4.3 Nanocavity Characterisation

### 4.3.1 Fabrication Results

To minimize losses during measurements the Au mirror should be as smooth as possible. Furthermore, a smooth film makes it much easier to identify nanoparticles at low magnification in the SEM and for the low-resolution extinction maps in the optical set up. The spacer layer will follow the Au surface, so it is crucial to have a smooth mirror layer. The base piranha and plasma cleaning steps were taken as precautions to ensure that the substrates were clean and free of contaminants to ensure smooth deposition of the following layers. Figure 4.14 shows SEM images taken of three films fabricated on silicon substrates prepared using the same procedures described in 3.3.2 and 3.3.3 but the evaporation step varies. Figure 4.14a was evaporated using Polyteknik E-flex e-beam physical vapour deposition with 5 nm Cr adhesion and 200 nm Au, Figure 4.14b was evaporated using Polyteknik E-flex e-beam physical vapour deposition with 5 nm Ti adhesion and 100 nm Au, and Figure 4.14c was evaporated using Nanoontje thermal evaporation with 5 nm Cr adhesion and 100 nm Au. An adhesion layer is

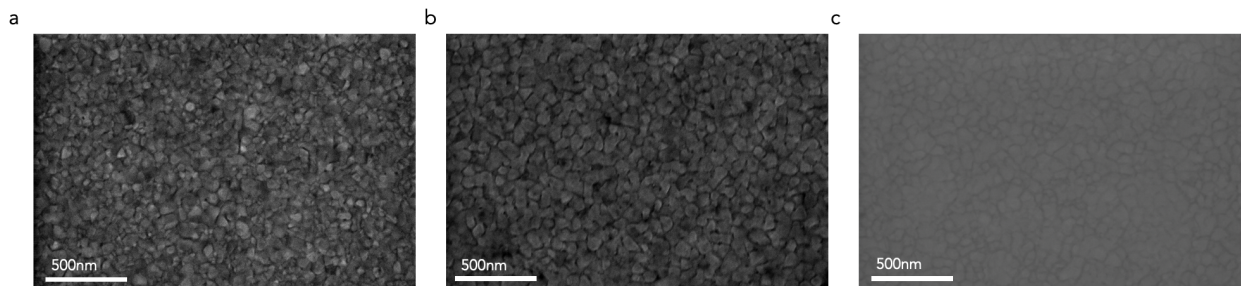


FIGURE 4.14: SEM images of Au mirror a. evaporated using Polyteknik E-flex e-beam physical vapour deposition with 5 nm Cr adhesion 5 nm Au b. evaporated using Polyteknik E-flex e-beam physical vapour deposition with 5 nm Ti adhesion 5 nm Au c. evaporated using Nanoontje thermal evaporation with 5 nm Cr adhesion 5 nm Au

required due to Au being a noble metal which therefore does not form intermetallic oxide layers and does not adhere to silicon substrates well which have an  $\text{SiO}_2$  layer on the surface. Conversely, both titanium (Ti) and chromium (Cr) bond easily with the oxide layer thus have a strong adhesion to the substrate [81]. When the Au is deposited on the metallic Ti or Cr an alloy is formed with a high bonding strength. As more layers of Au are deposited the film becomes pure Au. From the results in Figure 4.14, although not quantitative, it is evident from the contrast visible in the SEM that Figure 4.14a has a rough surface. Cr and Ti were tested as adhesion layers, with Ti showing less contrast in Figure 4.14b than for Cr Figure 4.14a, but is still too rough for the optical measurements to follow. Finally, a different deposition method was

used, namely electric thermal evaporation as opposed to e-beam thermal evaporation. This film obtained from this method displays almost no contrast between the grains in Figure 4.14c.

One explanation for the difference in film quality between the e-beam evaporated and electric current evaporation is the purity of the targets. The targets are placed in boats days in advance of evaporation in the e-beam evaporator. Perhaps due to evaporation of other materials the Au target could become contaminated. Whereas, in the Nanoontje, the user directly inputs the required amount of pellets into the boats and then into the evaporator for immediate use, thus decreasing the chance of contamination.

### 4.3.2 Quality Factor

After the ligand exchange was carried out, cavities with 20 cycles of ALD ( $\approx 3$  nm  $\text{Al}_2\text{O}_3$ ) were characterised. Measurements for an Au and Au@Pd nanocavity were taken for comparison. Figure 4.15a,b display the measured Au and Au@Pd gap plasmon

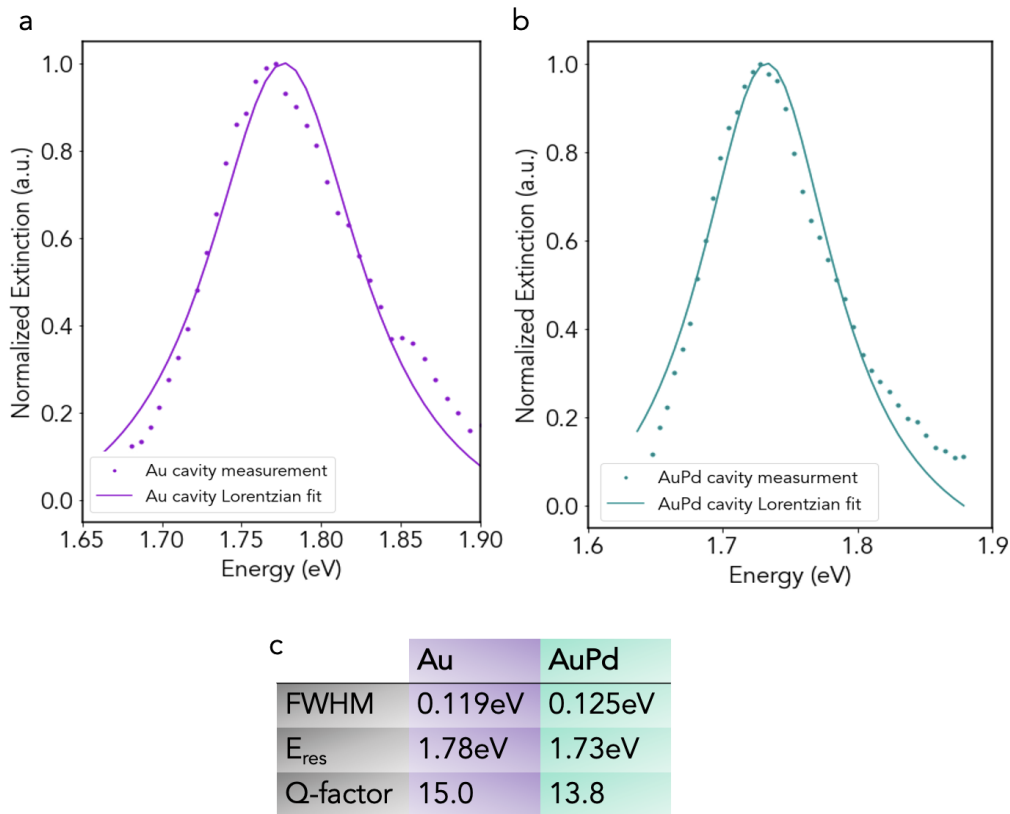


FIGURE 4.15: Measured and Lorentzian fit of a. Au cavity and b. Au@Pd cavity c. FWHM,  $E_{res}$  and Q factor obtained from fit

resonance respectively with a Lorentzian fit. As discussed in section 2.2.5, applying a



Lorentzian fit enables the extraction of the FWHM and  $E_{res}$ . Using these values the Q factor can be calculated according to,

$$Qfactor = \frac{E_{res}}{FWHM} \quad (4.1)$$

The Q factor for Au and Au@Pd cavities was calculated to be 15.8 and 13 respectively. For an  $\approx 70$  nm Au nanocube on mirror Oksenberg et al. obtained a Q factor of 27.9 [38]. The nanocube in that measurement was capped with citrates, whereas in this work both the Au and Au@Pd NCoMS have MBA adsorbed to the surface. The lower Q factor obtained for the Au nanocavity in this work is probably due to the different ligands on nanocube which can drastically change the FWHM and  $E_{res}$ .

Nevertheless, it is extremely promising for the Au@Pd NCoM that the Q factor obtained is comparable to that of the Au NCoM. The Au@Pd cavity has a resonant energy of  $1.73 \text{ eV} \approx 717 \text{ nm}$  for an  $\approx 3 \text{ nm}$  spacer. According to simulations shown in Figure 4.13 the resonant wavelength for this spacer and Pd shell thickness should be further into the near-IR at  $\approx 790 \text{ nm}$ . However, the simulations do not account for ligands on the nanocube which make the effective spacer thicker, which explains the blue shift observed in experiment. Furthermore, although the mean size of the nanocubes was input in the simulation, the cube core and shell in this nanocavity could be smaller or larger than the mean values, which can alter the resonant energy.

### 4.3.3 NCoM Modes

CL spectra were measured to understand how the modes change spatially throughout the Au@Pd NCoM. Due to the sample charging, the spatial resolution is low, and the black squares on the left side of figure 4.16 are due to some measurement artefact. Nevertheless, this measurement is included to show how CL maps and spatially resolved spectra can be a useful tool to understand more about the Au@Pd interface. Figure 4.16 shows that the two highest peaks for the gap mode ( $\approx 690 \text{ nm}$ ) are the orange and purple spectra, obtained from pixels taken from the top left and bottom left corners (see inset). The gap resonances obtained from pixels on the right corners are lower, which was consistent for all spectra taken from all pixels on this side. Perhaps the cube was not lying completely flat on the mirror, and the left side could couple better to the cavity, or since the thickness of the shell is non uniform, perhaps it is thicker on the right side of the cube.

Figure 4.17a shows an SEM image of the cube which the CL measurements were conducted, accompanied with the CL map of the interband mode shown in Figure 4.17 e and the gap mode in Figure 4.17c both with a bandwidth of 30 nm. Similar to the cube showing the interband mode in Figure 2.8, 4 bright spots can be seen in Figure

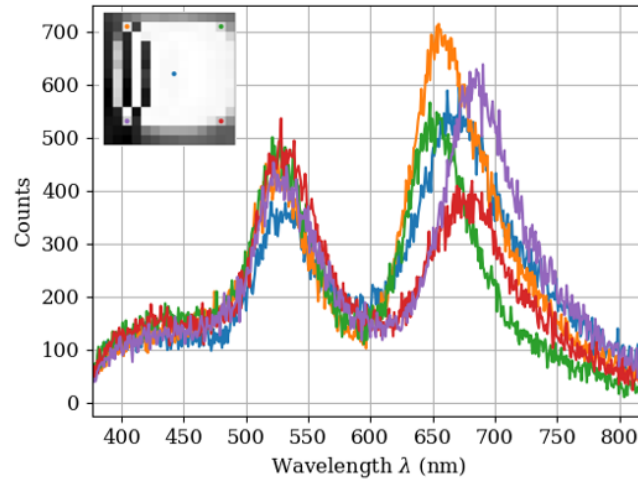


FIGURE 4.16: CL spectra of Au@Pd NCoM taken at different positions on cube (inset)

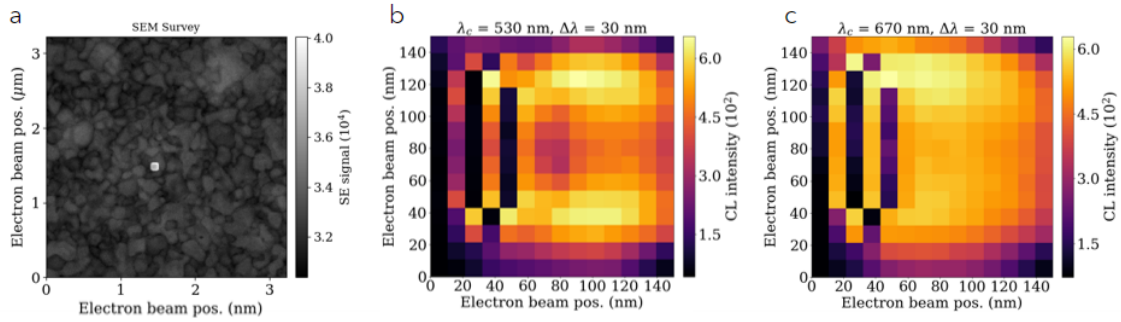


FIGURE 4.17: a. SEM image of Au@Pd NCoM b. CL map of modes at 530 nm with 30 nm band width c. CL map of modes at 670 nm with 30 nm band width

4.17b. These bright areas could represent the 4 corners of the nanocube, however due to the low spatial resolution it can not be confirmed. Figure 4.17c resembles the gap mode shown in Figure 2.8, with the bright fringes along the top and bottom of the cube. Again, these measurements do not provide concrete evidence of the modes observed in the Au@Pd NCoM but they do hint towards the results observed in literature for modes in these systems.

## 4.4 Plasmon Driven Chemistry

### 4.4.1 Controls

Prior to inducing reactions in the nanocavities, it is important to carry out control measurements. Due to time constraints of this project, some control measurements were not taken. However, it is critical to discuss the steps that should be carried out preceding future reaction experiments so that more exact and quantitative data can be extracted from the measurements.

#### Conduct Linescans on Cavities Prior to Ligand Exchange

The plasmon resonance lineshape is sensitive not only to chemical changes but also structural changes in the nanocube itself. The Au cubes are citrate capped and the Au@Pd cubes are CTAB capped. These capping ligands are not expected to undergo reactions under 10 consecutive wavelength scans. Therefore large changes in the lineshape are not expected with these capping agents on the surface (prior to ligand exchange) [38] If large changes are observed in the lineshape over 10 consecutive scans with just citrates or CTAB on the surface of the cube, the lineshape change could simply be due to structural changes on the cube. Therefore, it cannot be said for measurements to follow that it is truly a reaction inducing changes in the lineshape unless this control is performed. Furthermore, once the gap plasmon resonance energy is known, only the required wavelengths of the gap mode can be probed to induce the reaction. This results in avoiding the need to include wavelengths close to Au interband excitations in the wavelength scan.

#### Surface Enhanced Raman Spectroscopy Measurement to Confirm Ligand Exchange

Although the ligand exchange protocol that was followed is an overshoot for the required time for the ligand exchange followed by other groups [67–69], surface enhanced raman spectroscopy (SERS) should be used to identify the metal-bound molecules. Both CTAB and MBA have distinct Raman spectra, therefore it would be discernible if the exchange was successful. This technique can be used due to the enhanced near field generated by the plasmonic nanostructure and so on resonance measurements provide the strongest signal.

#### Induce Reaction on Au Nanocavities

To claim that the Pd shell improves catalysis, control reactions should also be conducted on Au nanocavities. This would uncover if the Au@Pd enhances reaction rates

compared to Au, and further that the Au@Pd cavity may unlock a completely new reaction pathway compared to bare Au.

#### 4.4.2 Measurements

Measurements were carried out on Au@Pd cavities with a  $\approx 3$  nm spacer layer. Measurements were induced and monitored on 5 individual nanocavities by conducting 10 consecutive wavelength scans from 500-780 nm on each cavity as shown in Figure 4.18a.

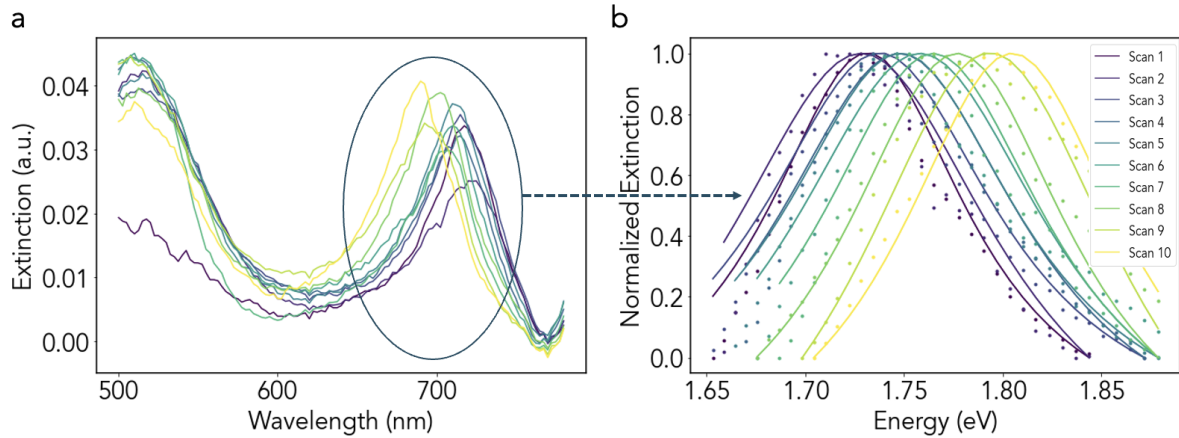


FIGURE 4.18: a. Raw reaction data from 10 consecutive wavelength scans on single nanocavity from 500 - 780 nm. b. Extracted gap plasmon resonance from a with Lorentzian fit

Figure 4.18b displays how the gap resonance is extracted from the data, put on an energy scale, and fitted with a Lorentzian to obtain the FWHM and  $E_{res}$  for each scan. The other cavity measurements are in the appendix.

#### Measurement Analysis

To resolve the process on an energy scale, the change in FWHM between the 1<sup>st</sup> and 10<sup>th</sup> scan ( $\Delta\Gamma_{res}$ ) vs. the resonant energy of the 1<sup>st</sup> scan ( $E_{res}$ ) is plotted and is displayed in Figure 4.19a. Similarly, the change in resonant energy between the 1<sup>st</sup> and 10<sup>th</sup> scan ( $\Delta E_{res}$ ) vs. the resonant energy of the 1<sup>st</sup> scan ( $E_{res}$ ) is plotted in Figure 4.19b. Each square represents a single cavity.

Before using this data to make claims about if and what reaction is happening, and furthermore what the baseline noise level is, it is important to check if changes in the FWHM and  $E_{res}$  are consistent throughout the scans. A change between the 1<sup>st</sup> and 10<sup>th</sup> scan is expected, however changes in the interim should be in the same direction. Figure 4.20a shows the FWHM obtained from each scan for 5 cavities. There is no clear trend in the FWHM from the 1<sup>st</sup> to 10<sup>th</sup> scan as the FWHM oscillates from scan

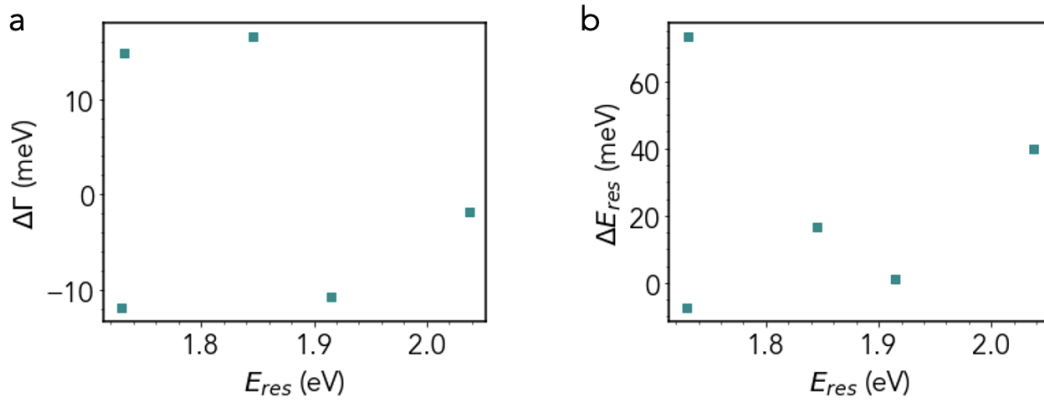


FIGURE 4.19: (a) Change in FWHM between the 1<sup>st</sup> and 10<sup>th</sup> scan ( $\Delta\Gamma_{res}$ ) vs. the resonant energy of the 1<sup>st</sup> scan ( $E_{res}$ ) (b) Change in resonant energy between the 1<sup>st</sup> and 10<sup>th</sup> scan ( $\Delta E_{res}$ ) vs. the resonant energy of the 1<sup>st</sup> scan ( $E_{res}$ ). Each square represents a single cavity.

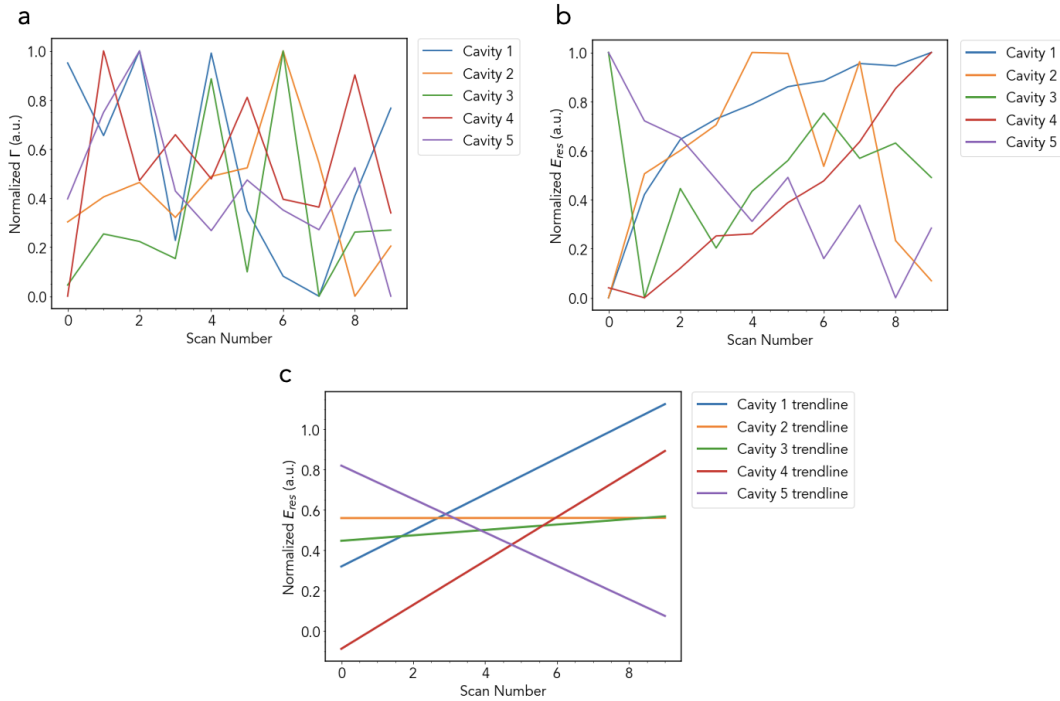


FIGURE 4.20: a Normalized FWHM plotted for each cavity for each scan b Normalized resonant energy plotted for each cavity for each scan c Trendline obtained for normalized resonant energy plotted for each cavity for each scan

to scan. The changes observed are due to poor Lorentzian fitting of the measurements because the low signal of the measurements. Moreover, the Pd shell makes the curve less 'Lorentzian' in shape, and so the fitting is not perfect. The fitting quality varied a lot from scan to scan. This means that some scans had a good fit and others had a

poor fit. The change in quality of the fitting for each scan means that any changes seen in the FWHM cannot be taken as data that can be used to understand the reaction process.

However, in Figure 4.20b, there is a trend observed for the change in resonant energy throughout the scans for cavity 1, 4 and 5. The Lorentzian fitting was much more stable for acquiring the correct resonant energy. Figure 4.20c shows the plotted trend lines for the normalized  $E_{res}$ , which for cavity 1 and 4 is increasing, thus a blue shift in resonant energy is induced by the process happening at the surface. Although cavity 3 is unstable, in general the trend is also blue shifting. As discussed in section 2.2.4, assuming changes in the lineshape are due to a reaction, a blue shift implies that the product is more electron withdrawing than the reactant or that the reactant desorbed from the nanoparticle. Since the COOH group of MBA is already strongly electron withdrawing, the product must have an even stronger withdrawing group. This could include an aldehyde or ester. Cavity 5 also has some instability but overall, the trend decreases, meaning that the process is inducing a red shift in resonant energy. This suggests that the product is more electron donating than the reactant. This could be the MBA undergoing decarboxylation to produce thiophenol. This reaction is commonly observed on plasmonic Au at 785 nm [67–69]. The COOH group is replaced with a H, which is less electron withdrawing. Cavity 2 does not seem to follow any trend. However due to the varying resonant energies of the cavities in this work it is possible to have different chemical reactions assuming that the reaction pathway is energy dependent.

## Chapter 5

# Conclusions and Outlook

Au@Pd NCoMs have shown to be a promising route for studying plasmon driven chemistry. Despite the plasmon damping due to the Pd shell, a strong and relatively sharp gap plasmon resonance is observed, with a quality factor of 13.8. Due to time constraints of the project all necessary controls prior to reaction measurements were not taken. During the measurement analysis it was assumed that a reaction took place in the cavity, although due to the lack of control measurements this cannot be confirmed. In future work on the system these should be performed before inducing reactions.

Furthermore, according to simulations, a wide range of resonant energies can be targeted by changing the thickness of the spacer. Many more measurements (in the order of hundreds) should be taken with a range of spacer thicknesses to span the VIS-NIR range to obtain a full picture of the MBA reactivity landscape. Cavities with resonant energies that match the resonant energies shown to exhibit large changes in the lineshape in the reactivity landscape should then be identified. These cavities can be probed using SERS to identify the products of the reaction at those energies. By combining the reactivity landscape of MBA with SERS measurements the reaction mechanism could be understood.

Nevertheless, the Au@Pd NCoM is a suitable platform for hydrogen detection. The narrow gap plasmon resonance allows for high resolution for detecting small changes in hydrogen concentrations. For subsequent studies on the system, an experiment could be conducted to first check the sensitivity of the Au@Pd NCoM to changes in concentration of hydrogen gas flow by tracking changes induced to the lineshape. Moreover, the detection limit of the sensor could be discovered by using very low concentrations of hydrogen to test at what point changes in the lineshape are no longer observed. Also, it would be interesting to see if there is a particular cavity resonance energy that is more sensitive to hydrogen adsorption and desorption.

Although, this work has not explored the enhanced plasmonic photocatalysis enabled by the Au@Pd NCoM compared with a Au NCoM, the cavities are ready to conduct these measurements. Formic acid dehydrogenation would be an interesting reaction to study as it has been proposed as a hydrogen storage material. Colloidal

Au@Pd nanorods have shown enhanced and selective formic acid dehydrogenation. However, studying the process in a Au@Pd NCoM would be insightful to explore the dependence of the reaction pathway, rate and selectivity on the resonant energy of the cavity probed.

Moreover, conducting more CL measurements on the cavities would uncover how the modes change spatially in the Au@Pd NCoM structure with varying shell thicknesses and spacer thicknesses. These results could shed light on how the plasmon resonances behave at the interface of the metals.

In conclusion, the Au@Pd NCoM is an interesting system from both a fundamental and applied standpoint, and there are many more exciting experiments to be carried out to unlock the potential of this system.



# Bibliography

- [1] Andrei A. Zagorodni. “Chapter 18 - Subjects that do not Fit in Other Chapters”. In: *Ion Exchange Materials*. Ed. by Andrei A. Zagorodni. Oxford: Elsevier, 2007, pp. 377–395. ISBN: 978-0-08-044552-6. DOI: <https://doi.org/10.1016/B978-008044552-6/50019-8>. URL: <https://www.sciencedirect.com/science/article/pii/B9780080445526500198>.
- [2] Zhi Li et al. “Well-Defined Materials for Heterogeneous Catalysis: From Nanoparticles to Isolated Single-Atom Sites”. In: *Chemical Reviews* 120.2 (2019), pp. 623–682. DOI: 10.1021/acs.chemrev.9b00311.
- [3] M Boudart. “Heterogeneous catalysis by metals”. In: *Journal of Molecular Catalysis* 1986 (1986), pp. 29–41. DOI: 10.1016/0304-5102(86)89003-4.
- [4] Tiffany Vass et al. *Chemicals – Analysis - IEA*. 2021. URL: <https://www.iea.org/reports/chemicals>.
- [5] H.-O Pörtner et al. *IPCC, 2022: Climate Change 2022: Impacts, Adaptation, and Vulnerability. Contribution of Working Group II to the Sixth Assessment Report of the Intergovernmental Panel on Climate Change*. Cambridge University Press, 2022.
- [6] Masson Delmotte et al. *Glossary*. 2018.
- [7] Hui-Shu Feng et al. “In situ investigation of hot-electron-induced SuzukiMiyaura reaction by surface-enhanced Raman spectroscopy”. In: *Journal of Applied Physics* 128.17 (2020), p. 173105. DOI: 10.1063/5.0023623.
- [8] William L. Barnes, Alain Dereux, and Thomas W. Ebbesen. “Surface plasmon subwavelength optics”. In: *Nature* 424.6950 (2003), pp. 824–830. DOI: 10.1038/nature01937.
- [9] Anushree Dutta et al. “Kinetics and Mechanism of Plasmon-Driven Dehalogenation Reaction of Brominated Purine Nucleobases on Ag and Au”. In: *ACS Catalysis* 11.13 (2021), pp. 8370–8381. DOI: 10.1021/acscatal.1c01851.
- [10] Stefan A. Maier. *Plasmonics: Fundamentals and Applications*. 1st ed. Springer, 2007.

- 
- [11] Allison M. Marn et al. “Multiplexed, High-Sensitivity Measurements of Antibody Affinity Using Interferometric Reflectance Imaging Sensor”. In: *Biosensors* 11.12 (2021), p. 483. DOI: 10.3390/bios11120483.
- [12] S Kamba et al. *Dielectric dispersion of the relaxor PLZT ceramics in the frequency range 20 Hz-100 THz*.
- [13] Lukas Novotny and Bert Hecht. *Principles of nano-optics*. Cambridge University Press, 2019.
- [14] Xiao Zhang et al. “Product selectivity in plasmonic photocatalysis for carbon dioxide hydrogenation”. In: *Nature Communications* 8.1 (2017). DOI: 10.1038/ncomms14542.
- [15] Sven Askes and Erik Garnett. “Ultrafast Thermal Imprinting of Plasmonic Hotspots”. In: *Advanced Materials* 33 (Dec. 2021). DOI: 10.1002/adma.202105192.
- [16] Elizabeth R. Hopper et al. “Opportunities and Challenges for Alternative Nanoplasmonic Metals: Magnesium and Beyond”. In: *The Journal of Physical Chemistry C* (2022). DOI: 10.1021/acs.jpcc.2c01944.
- [17] Ruben F. Hamans, Rifat Kamarudheen, and Andrea Baldi. “Single Particle Approaches to Plasmon-Driven Catalysis”. In: *Nanomaterials* 10.12 (2020), p. 2377. DOI: 10.3390/nano10122377.
- [18] Zhaoke Zheng, Takashi Tachikawa, and Tetsuro Majima. “Plasmon-Enhanced Formic Acid Dehydrogenation Using Anisotropic Pd–Au Nanorods Studied at the Single-Particle Level”. In: *Journal of the American Chemical Society* 137.2 (2015), pp. 948–957. DOI: 10.1021/ja511719g.
- [19] Siwei Li et al. “Recent Advances in Plasmonic Nanostructures for Enhanced Photocatalysis and Electrocatalysis”. In: *Advanced Materials* 33 (Feb. 2021). DOI: 10.1002/adma.202000086.
- [20] Chao Zhan, Martin Moskovits, and Zhong-Qun Tian. “Recent Progress and Prospects in Plasmon-Mediated Chemical Reaction”. In: *Matter* 3 (July 2020), pp. 42–56. DOI: 10.1016/j.matt.2020.03.019.
- [21] Chao Zhan et al. “From plasmon-enhanced molecular spectroscopy to plasmon-mediated chemical reactions”. In: *Nature Reviews Chemistry* 2.9 (2018), pp. 216–230. DOI: 10.1038/s41570-018-0031-9.
- [22] Christian Frischkorn and Martin Wolf. “Femtochemistry at Metal Surfaces: Nonadiabatic Reaction Dynamics”. In: *Chemical Reviews* 106.10 (2006), pp. 4207–4233. DOI: 10.1021/cr050161r.

- [23] Masatoshi Osawa et al. “Surface-Enhanced Infrared Spectroscopy: The Origin of the Absorption Enhancement and Band Selection Rule in the Infrared Spectra of Molecules Adsorbed on Fine Metal Particles”. In: *Applied Spectroscopy* 47.9 (1993), pp. 1497–1502. DOI: 10.1366/0003702934067478.
- [24] Jon A. Schuller et al. “Plasmonics for extreme light concentration and manipulation”. In: *Nature Materials* 9.3 (2010), pp. 193–204. DOI: 10.1038/nmat2630.
- [25] Peter Zijlstra, Michel Orrit, and A. Femius Koenderink. “Metal Nanoparticles for Microscopy and Spectroscopy”. In: *Nanoparticles* (2014), pp. 53–98. DOI: 10.1007/978-3-662-44823-6\_3.
- [26] Cecilia Noguez. “Surface Plasmons on Metal Nanoparticles: The Influence of Shape and Physical Environment”. In: *The Journal of Physical Chemistry C* 111.10 (2007), pp. 3806–3819. DOI: 10.1021/jp066539m.
- [27] Zhicong He et al. “Principle and Applications of the Coupling of Surface Plasmons and Excitons”. In: *Applied Sciences* 10.5 (2020), p. 1774. DOI: 10.3390/app10051774.
- [28] Chao Zhan, Martin Moskovits, and Zhong-Qun Tian. “Recent Progress and Prospects in Plasmon-Mediated Chemical Reaction”. In: *Matter* 3.1 (2020), pp. 42–56. DOI: 10.1016/j.matt.2020.03.019.
- [29] Mark Brongersma, Naomi Halas, and Peter Nordlander. “Plasmon-induced hot carrier science and technology”. In: *Nature nanotechnology* 10 (Jan. 2015), pp. 25–34. DOI: 10.1038/nnano.2014.311.
- [30] Rajkumar Devasenathipathy et al. “Plasmonic Photoelectrochemical Coupling Reactions of para -Aminobenzoic Acid on Nanostructured Gold Electrodes”. In: *Journal of the American Chemical Society* 144 (Feb. 2022). DOI: 10.1021/jacs.1c10447.
- [31] Yuchao Zhang et al. “Surface-Plasmon-Driven Hot Electron Photochemistry”. In: *Chemical Reviews* 118.6 (2017), pp. 2927–2954. DOI: 10.1021/acs.chemrev.7b00430.
- [32] Gregory Hartland et al. “What’s so Hot about Electrons in Metal Nanoparticles?”. In: *ACS Energy Letters* 2 (June 2017). DOI: 10.1021/acseenergylett.7b00333.
- [33] Zhandong Li and Dmitry Kurovski. “Nanoscale structural characterization of plasmon-driven reactions”. In: *Nanophotonics* 10.6 (2021), pp. 1657–1673. DOI: 10.1515/nanoph-2020-0647.

- [34] Alexander O. Govorov, Hui Zhang, and Yurii K. Gun'ko. "Theory of Photoinjection of Hot Plasmonic Carriers from Metal Nanostructures into Semiconductors and Surface Molecules". In: *The Journal of Physical Chemistry C* 117.32 (2013), pp. 16616–16631. DOI: 10.1021/jp405430m.
- [35] Calvin Boerigter, Umar Aslam, and Suljo Linic. "Mechanism of Charge Transfer from Plasmonic Nanostructures to Chemically Attached Materials". In: *ACS Nano* 10.6 (2016), pp. 6108–6115. DOI: 10.1021/acsnano.6b01846.
- [36] Guillaume Baffou et al. "Simple experimental procedures to distinguish photothermal from hot-carrier processes in plasmonics". In: *Light: Science and Applications* 9.1 (2020). DOI: 10.1038/s41377-020-00345-0.
- [37] Thang B. Hoang et al. "Ultrafast spontaneous emission source using plasmonic nanoantennas". In: *Nature Communications* 6.1 (2015). DOI: 10.1038/ncomms8788.
- [38] Eitan Oksenberg et al. "Energy-resolved plasmonic chemistry in individual nanoreactors". In: *Nature Nanotechnology* 16.12 (2021), pp. 1378–1385. DOI: 10.1038/s41565-021-00973-6.
- [39] Volker J. Sorger et al. "Plasmonic Fabry-Pérot Nanocavity". In: *Nano Letters* 9.10 (2009), pp. 3489–3493. DOI: 10.1021/nl901682n.
- [40] Jeremy J. Baumberg et al. "Extreme nanophotonics from ultrathin metallic gaps". In: *Nature Materials* 18.7 (2019), pp. 668–678. DOI: 10.1038/s41563-019-0290-y.
- [41] Rohit Chikkaraddy et al. "How Ultranarrow Gap Symmetries Control Plasmonic Nanocavity Modes: From Cubes to Spheres in the Nanoparticle-on-Mirror". In: *ACS Photonics* 4.3 (2017), pp. 469–475. DOI: 10.1021/acsp Photonics.6b00908.
- [42] Tao Ding et al. "Capillary-Force-Assisted Optical Tuning of Coupled Plasmons". In: *Advanced Materials* 27.41 (2015), pp. 6457–6461. DOI: 10.1002/adma.201503292.
- [43] Nuttawut Kongsuwan et al. "Plasmonic Nanocavity Modes: From Near-Field to Far-Field Radiation". In: *ACS Photonics* 7.2 (2020), pp. 463–471. DOI: 10.1021/acsp Photonics.9b01445.
- [44] Matthew E. Sykes et al. "Enhanced generation and anisotropic Coulomb scattering of hot electrons in an ultra-broadband plasmonic nanopatch metasurface". In: *Nature Communications* 8.1 (2017). DOI: 10.1038/s41467-017-01069-3.
- [45] Oleg A. Yeshchenko et al. "Size and Temperature Effects on the Surface Plasmon Resonance in Silver Nanoparticles". In: *Plasmonics* 7.4 (2012), pp. 685–694. DOI: 10.1007/s11468-012-9359-z.

- [46] Jing Niu et al. “Shifting of surface plasmon resonance due to electromagnetic coupling between graphene and Au nanoparticles”. In: *Optics Express* 20.18 (2012), p. 19690. DOI: 10.1364/oe.20.019690.
- [47] Shengxi Huang et al. “Ultrasmall Mode Volumes in Plasmonic Cavities of Nanoparticle-On-Mirror Structures”. In: *Small* 12.37 (2016), pp. 5190–5199. DOI: 10.1002/smll.201601318.
- [48] Stephen A. Lee and Stephan Link. “Chemical Interface Damping of Surface Plasmon Resonances”. In: *Accounts of Chemical Research* 54.8 (2021), pp. 1950–1960. DOI: 10.1021/acs.accounts.0c00872.
- [49] H. Hövel et al. “Width of cluster plasmon resonances: Bulk dielectric functions and chemical interface damping”. In: *Phys. Rev. B* 48 (24 1993), pp. 18178–18188. DOI: 10.1103/PhysRevB.48.18178. URL: <https://link.aps.org/doi/10.1103/PhysRevB.48.18178>.
- [50] Thakshila Liyanage et al. “Reversible Tuning of the Plasmoelectric Effect in Noble Metal Nanostructures Through Manipulation of Organic Ligand Energy Levels”. In: *Nano Letters* 20.1 (2019), pp. 192–200. DOI: 10.1021/acs.nanolett.9b03588.
- [51] Dayne F. Swearer et al. “Heterometallic antennareactor complexes for photocatalysis”. In: *Proceedings of the National Academy of Sciences* 113.32 (2016), pp. 8916–8920. DOI: 10.1073/pnas.1609769113.
- [52] Abhijit Roy, Diptiranjana Paital, and Saumyakanti Khatua. “Pd-Coated Au Triangular Nanoprisms as Catalysts for Hot-Carrier-Driven Photochemistry”. In: *ACS Applied Nano Materials* 5.3 (2022), pp. 4437–4446. DOI: 10.1021/acsanm.2c00534.
- [53] Pin Lyu et al. “Mechanistic insight into deep holes from interband transitions in Palladium nanoparticle photocatalysts”. In: *iScience* 25.2 (2022), p. 103737. DOI: 10.1016/j.isci.2022.103737.
- [54] Michael Nathanson et al. “Atomic-Scale Structure and Stress Release Mechanism in Core–Shell Nanoparticles”. In: *ACS Nano* 12.12 (2018), pp. 12296–12304. DOI: 10.1021/acsnano.8b06118.
- [55] Zhandong Li, Rui Wang, and Dmitry Kurovski. “Nanoscale Photocatalytic Activity of Gold and Gold–Palladium Nanostructures Revealed by Tip-Enhanced Raman Spectroscopy”. In: *The Journal of Physical Chemistry Letters* 11.14 (2020), pp. 5531–5537. DOI: 10.1021/acs.jpcclett.0c01631.

- [56] Jessi E. S. van der Hoeven et al. “Unlocking synergy in bimetallic catalysts by core–shell design”. In: *Nature Materials* 20.9 (2021), pp. 1216–1220. DOI: 10.1038/s41563-021-00996-3.
- [57] Emma Westsson, Stephen Picken, and Ger Koper. “The effect of lattice strain on catalytic activity”. In: *Chemical Communications* 55.9 (2019), pp. 1338–1341. DOI: 10.1039/c8cc09063g.
- [58] Yong Ding et al. “Atomic Structure of AuPd Bimetallic Alloyed Nanoparticles”. In: *Journal of the American Chemical Society* 132.35 (2010), pp. 12480–12486. DOI: 10.1021/ja105614q.
- [59] Zijun Yong et al. “Fine-Tuning Au@Pd Nanocrystals for Maximum Plasmon-Enhanced Catalysis”. In: *Advanced Materials Interfaces* 8.3 (2020), p. 2001686. DOI: 10.1002/admi.202001686.
- [60] “Effect of lattice mismatch and shell thickness on strain in core@shell nanocrystals”. In: 2 (). DOI: 10.1039/d0na00061b.
- [61] Zhenni Wang et al. “Lattice-Mismatch-Induced Twinning for Seeded Growth of Anisotropic Nanostructures”. In: *ACS Nano* 9.3 (2015), pp. 3307–3313. DOI: 10.1021/acsnano.5b00475.
- [62] Priyanka Verma et al. “Enhancement of plasmonic activity by Pt/Ag bimetallic nanocatalyst supported on mesoporous silica in the hydrogen production from hydrogen storage material”. In: *Applied Catalysis B: Environmental* 223 (2018), pp. 10–15. DOI: 10.1016/j.apcatb.2017.05.017.
- [63] Jörg Eppinger and Kuo-Wei Huang. “Formic Acid as a Hydrogen Energy Carrier”. In: *ACS Energy Letters* 2.1 (2016), pp. 188–195. DOI: 10.1021/acseenergylett.6b00574.
- [64] Nacer Boubiche et al. “Au–Pd core–shell nanoparticle film for optical detection of hydrogen gas”. In: *AIP Advances* 10.10 (2020), p. 105225. DOI: 10.1063/5.0023461.
- [65] M. W. EVANS. “Combustion, Flames and Explosions of Gases. Bernard Lewis and Guenther von Elbe. New York: Academic Press, 1951. 795 pp.” In: *Science* 115.2987 (1952), pp. 363–363. DOI: 10.1126/science.115.2987.363.
- [66] Ferry A. A. Nugroho et al. “Metal–polymer hybrid nanomaterials for plasmonic ultrafast hydrogen detection”. In: *Nature Materials* 18.5 (2019), pp. 489–495. DOI: 10.1038/s41563-019-0325-4.
- [67] Hyun Huh et al. “How Does a Plasmon-Induced Hot Charge Carrier Break a C–C Bond?” In: *ACS Applied Materials and Interfaces* 11.27 (2019), pp. 24715–24724. DOI: 10.1021/acsaami.9b05509.

- [68] Yi Zong et al. “Plasmon-induced decarboxylation of mercaptobenzoic acid on nanoparticle film monitored by surface-enhanced Raman spectroscopy”. In: *RSC Adv.* 4.60 (2014), pp. 31810–31816. DOI: 10.1039/c4ra03512g.
- [69] Qingfeng Zhang, Kexun Chen, and Hui Wang. “Hot-Hole-Induced Molecular Scissoring: A Case Study of Plasmon-Driven Decarboxylation of Aromatic Carboxylates”. In: *The Journal of Physical Chemistry C* 125.38 (2021), pp. 20958–20971. DOI: 10.1021/acs.jpcc.1c07177.
- [70] P. B. Johnson and R. W. Christy. “Optical Constants of the Noble Metals”. In: *Physical Review B* 6.12 (1972), pp. 4370–4379. DOI: 10.1103/physrevb.6.4370.
- [71] Edward D Palik. *Handbook of optical constants of solids*. Acad. Press, 2003.
- [72] Hao Jing and Hui Wang. “Controlled overgrowth of Pd on Au nanorods”. In: *CrystEngComm* 16.40 (2014), pp. 9469–9477. DOI: 10.1039/c4ce00601a.
- [73] Heinz-Helmut Perkampus. *UV-VIS Spectroscopy and Its Applications*. Springer Science Business Media, 2013, pp. 1–4.
- [74] Jack Y. Zhang et al. “Variable-angle high-angle annular dark-field imaging: application to three-dimensional dopant atom profiling”. In: *Scientific Reports* 5.1 (2015). DOI: 10.1038/srep12419.
- [75] Steven M. George. “Atomic Layer Deposition: An Overview”. In: *Chemical Reviews* 110.1 (2009), pp. 111–131. DOI: 10.1021/cr900056b.
- [76] Michael B Toffolo et al. “Cathodoluminescence and Laser-Induced Fluorescence of Calcium Carbonate: A Review of Screening Methods for Radiocarbon Dating of Ancient Lime Mortars”. In: *Radiocarbon* 62.3 (2020), pp. 545–564. DOI: 10.1017/rdc.2020.21.
- [77] F. J. García de Abajo. “Optical excitations in electron microscopy”. In: *Reviews of Modern Physics* 82.1 (2010), pp. 209–275. DOI: 10.1103/revmodphys.82.209.
- [78] Pabitra Das, Tapas Kumar Chini, and James Pond. “Probing Higher Order Surface Plasmon Modes on Individual Truncated Tetrahedral Gold Nanoparticle Using Cathodoluminescence Imaging and Spectroscopy Combined with FDTD Simulations”. In: *The Journal of Physical Chemistry C* 116.29 (2012), pp. 15610–15619. DOI: 10.1021/jp3047533.
- [79] M. P. Navas and R. K. Soni. “Laser-Generated Bimetallic Ag-Au and Ag-Cu Core-Shell Nanoparticles for Refractive Index Sensing”. In: *Plasmonics* 10.3 (2014), pp. 681–690. DOI: 10.1007/s11468-014-9854-5.
- [80] Do Youb Kim et al. “Au@Pd core-shell nanocubes with finely-controlled sizes”. In: *CrystEngComm* 15.17 (2013), p. 3385. DOI: 10.1039/c3ce40175h.

- 
- [81] William M. Abbott et al. “Comparison of Metal Adhesion Layers for Au Films in Thermoplasmonic Applications”. In: *ACS Applied Materials and Interfaces* 12.11 (2020), pp. 13503–13509. DOI: 10.1021/acsami.9b22279.



## *Acknowledgements*

It has been an absolute pleasure working in the Nanoscale Solar Cells group over the last year. I would like to firstly thank Erik, for accepting me to the group and for all the positivity and enthusiasm. I am truly grateful for my daily supervisor Eitan, who had a vast store of knowledge to share in this field, but also for teaching me how to communicate better (which I am still working on!).

Thanks to my office mates Sarah, Rohit and Hongyu, who always made time for a chit chat, and were always willing to help with any problem or question I had, without hesitation. Also, a special thanks to Sarah for lending me a monitor, which has played a defining role in my life over the last few weeks. When Rohit joined the group I got to share my love for plasmons with someone who is equally as hyped about them, which has been fun, thank you!. Daan and Linde, thanks for all the laughs and cheesey jokes, I look forward to the next four years together. Thanks Susan for always encouraging openness and honesty. I am always impressed by how quickly Marc Duursma can solve any issue, thank you, we are lucky to have you.

I would like to extend my thanks to the entire Nanoscale Solar Cells group, who have always been positive and helpful throughout my time at AMOLF. It was a pleasure to spend a week in Switzerland with all of you, and look forward to more group outings in the future. Thanks to my second examiner Esther, who has made the time to listen to my talk and read this thesis. Thanks to all the cleanroom staff and superusers who have taken time to train me and help trouble shoot any issues in experiments. Hollie, thanks for helping out by taking the CL measurements, and thank you for the emotional and technical support you have provided over the last few months. I will be forever thankful! I would also like to thank Hallie, Jasmin, Liam and Hollie, who have been like my family in Amsterdam making my time here great.

Finally, I would like to thank my family. Without you I would not be here. I am beyond thankful for all the love and support you have shown me throughout my life. A special thanks to mom and dad, who will always answer the phone just to hear me babble for 30 minutes, I am forever grateful to you.

## Appendix A

### Measurement Data from Section 4.4.2

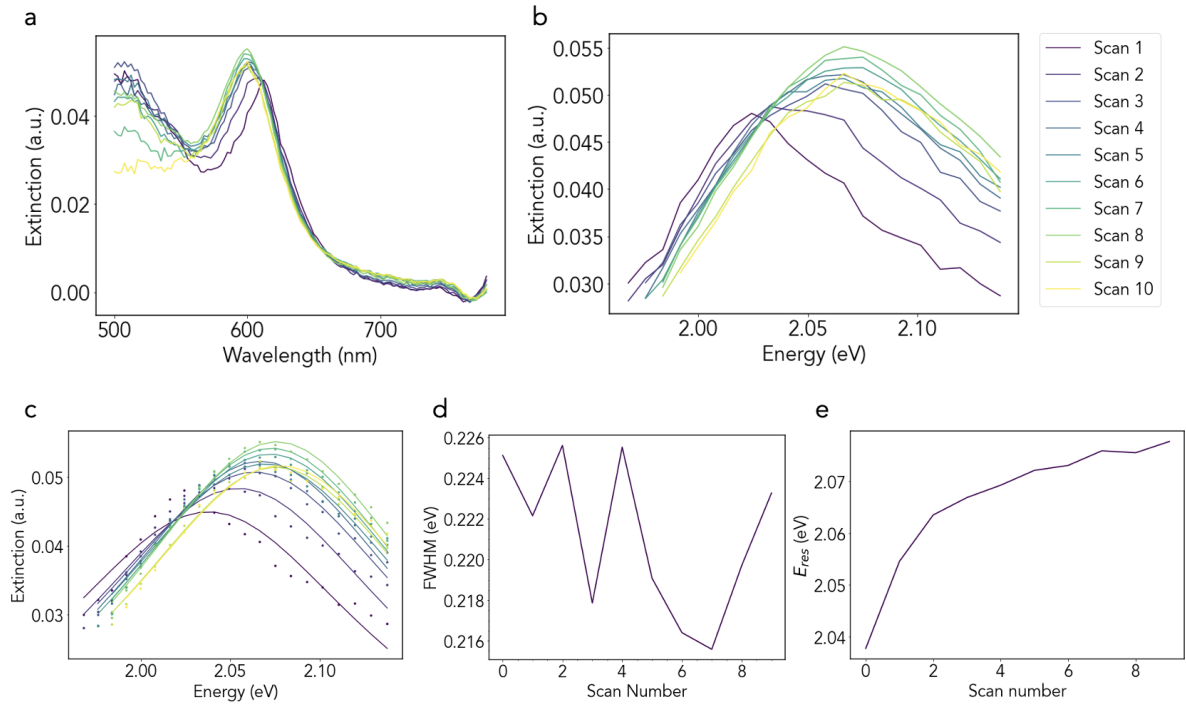


FIGURE A.1: Cavity 1: a. Measurement b. Gap resonance extraction c. Lorentzian fit of gap resonance d. FWHM for each scan e. Resonant energy for each scan

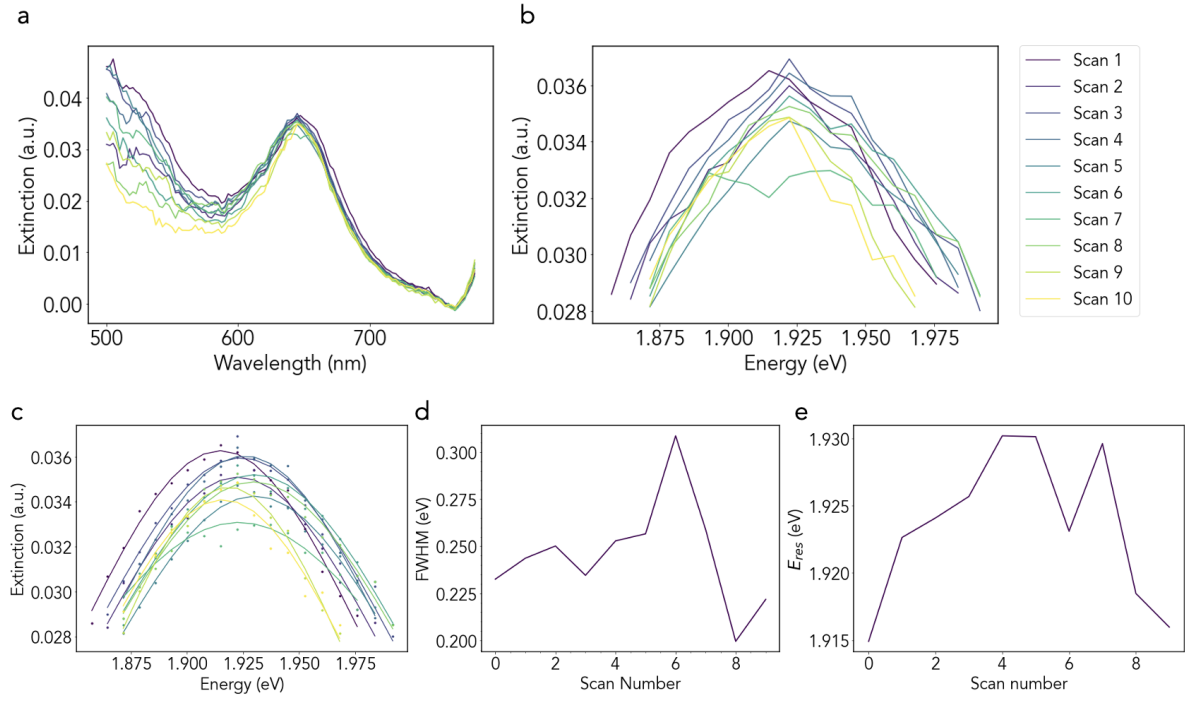


FIGURE A.2: Cavity 2: a. Measurement b. Gap resonance extraction c. Lorentzian fit of gap resonance d. FWHM for each scan e. Resonant energy for each scan

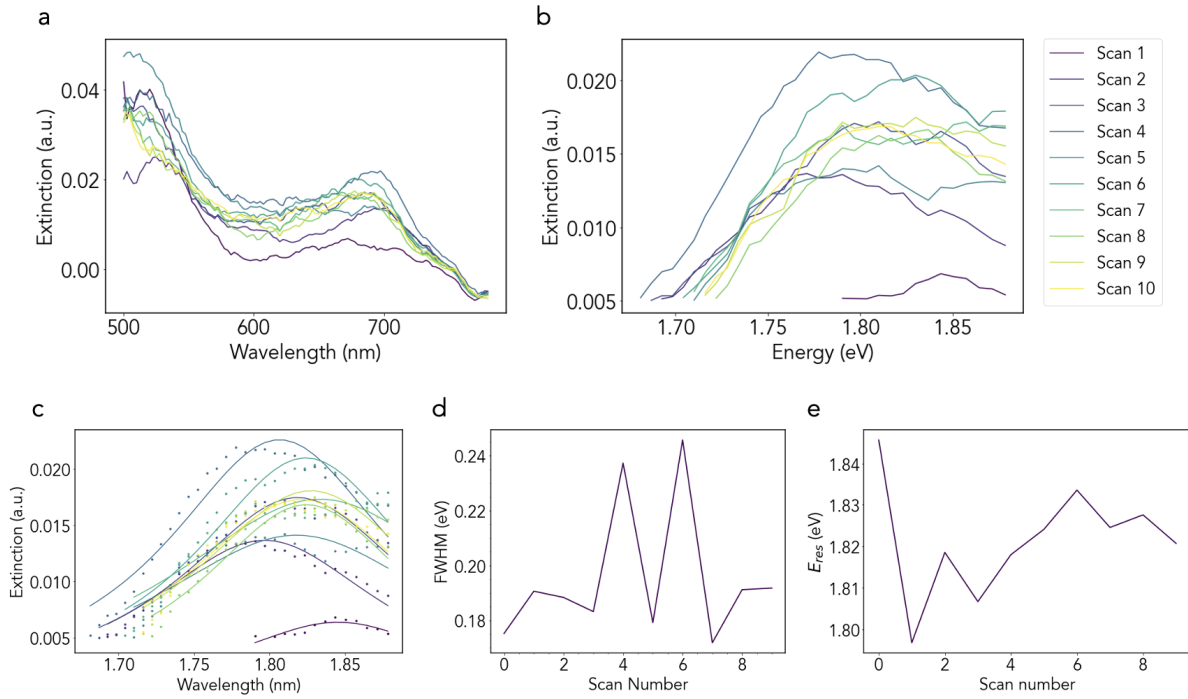


FIGURE A.3: Cavity 3: a. Measurement b. Gap resonance extraction c. Lorentzian fit of gap resonance d. FWHM for each scan e. Resonant energy for each scan

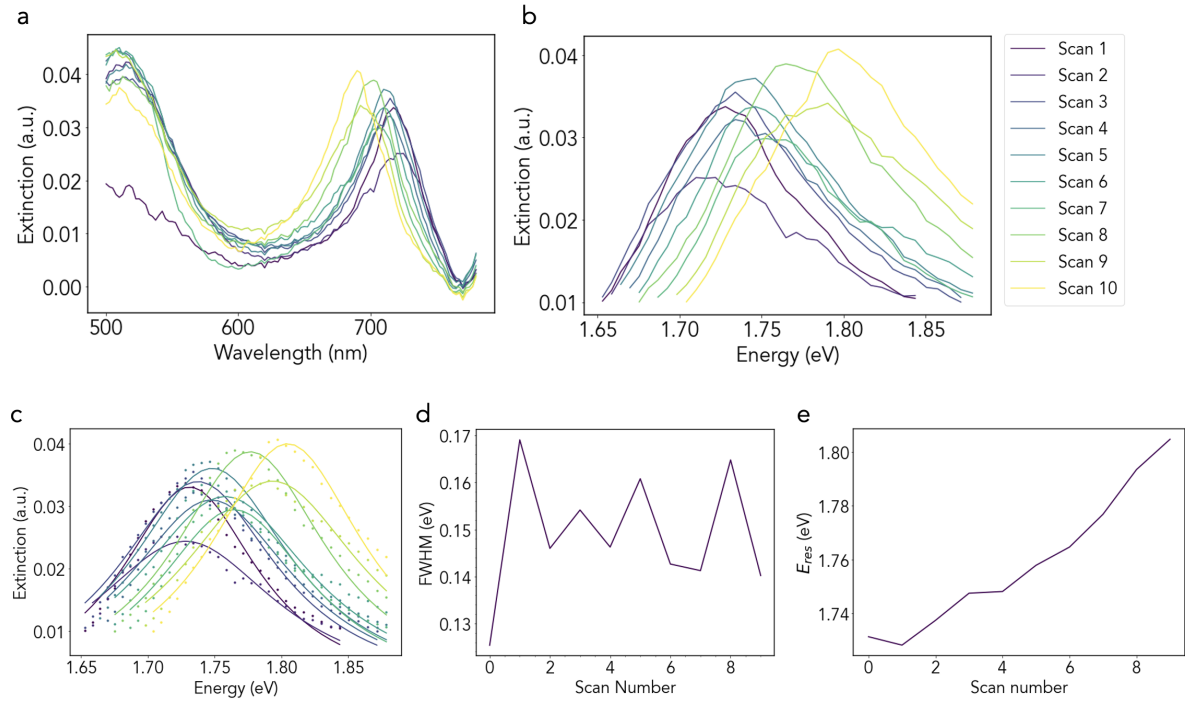


FIGURE A.4: Cavity 4: a. Measurement b. Gap resonance extraction c. Lorentzian fit of gap resonance d. FWHM for each scan e. Resonant energy for each scan

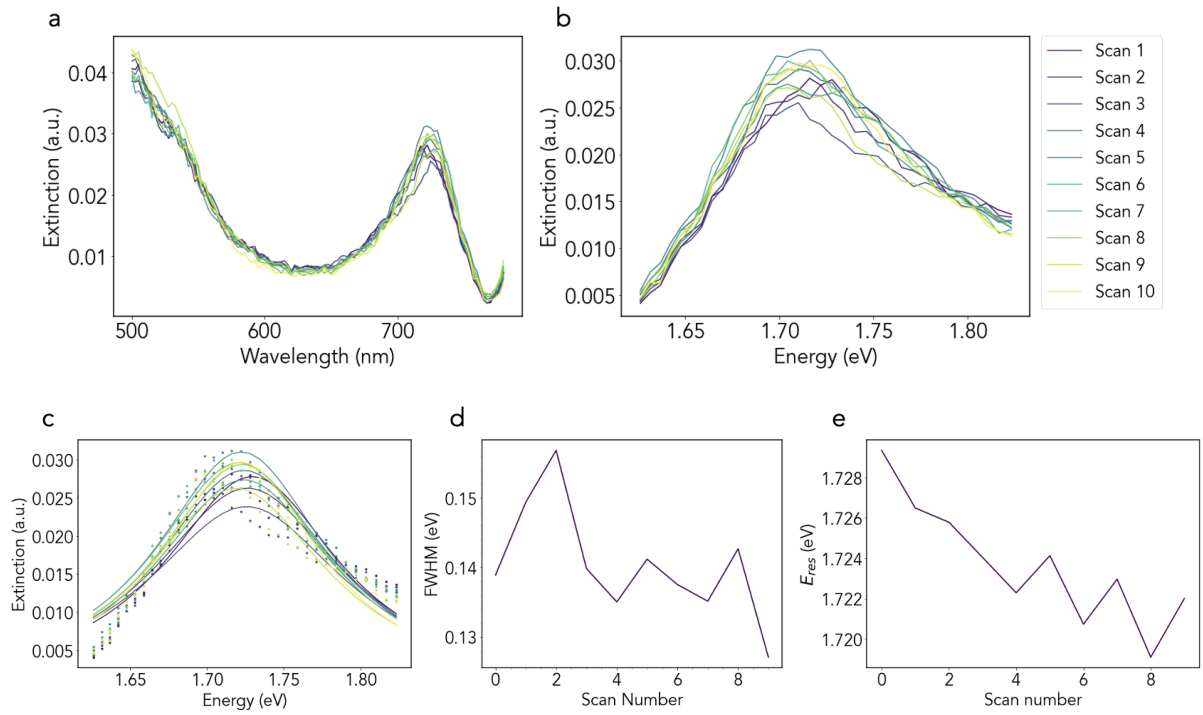


FIGURE A.5: Cavity 5: a. Measurement b. Gap resonance extraction c. Lorentzian fit of gap resonance d. FWHM for each scan e. Resonant energy for each scan